

# Impact of free-stream turbulence and thrust coefficient on wind turbine-generated wakes

Martin Bourhis <sup>1</sup>, Thomas Messmer <sup>2,3</sup>, Michael Hölling <sup>2,3</sup> and Oliver Buxton <sup>1</sup>

Corresponding authors: Martin Bourhis, m.bourhis@imperial.ac.uk; Oliver Buxton, o.buxton@imperial.ac.uk

(Received 31 March 2025; revised 30 September 2025; accepted 1 October 2025)

This study investigates the influence of free-stream turbulence (FST) and the thrust coefficient  $(C_T)$  on wind turbine wakes. Wakes generated at  $C_T \in \{0.5, 0.7, 0.9\}$  are exposed to turbulent inflows with varying FST intensities (1 %  $\lesssim$   $TI_{\infty} \lesssim$  11 %) and integral length scales  $(0.1 \lesssim \mathcal{L}_x/D \lesssim 2, D)$  is the rotor diameter). For high- $TI_{\infty}$  inflows, a flow region in the wake is observed where a mean momentum deficit persists despite the turbulence intensity having already homogenised with that of the free stream, challenging traditional wake definitions. A 'turning point' in the mean wake width evolution is identified, beyond which wakes spread at slower rates. Near-field  $(x/D \lesssim 7)$  wake growth rate increases with higher  $TI_{\infty}$  and  $C_T$ , while far-field  $(x/D \gtrsim 15)$  wake growth rate decreases with higher  $II_{\infty}$  – a finding with profound implications for wind turbine wake modelling that also aligns with the entrainment behaviours observed in bluff- and porousbody wakes exposed to FST. Increasing  $\mathcal{L}_x$  delays wake recovery onset and reduces the mean wake width, with minimal effect on the spreading rate. Both  $C_T$  and FST influence the high- and low-frequency wake dynamics, with varying contributions in the near and far fields. For low- $TI_{\infty}$  and small- $\mathcal{L}_x$  inflows, wake meandering is minimal, sensitive to C<sub>T</sub> and appears to be triggered by a shear-layer instability. Wake meandering is enhanced for high- $TI_{\infty}$  and large- $\mathcal{L}_x$  inflows, with the integral length scale playing a leading role. This emphasises the complex role of FST integral length scale: while increasing  $\mathcal{L}_x$ amplifies meandering, it does not necessarily translate to larger mean wake width due to the concurrent suppression of entrainment rate.

Key words: wakes, turbulent flows, turbulent mixing

<sup>&</sup>lt;sup>1</sup>Department of Aeronautics, Imperial College London, London SW7 2AZ, UK

<sup>&</sup>lt;sup>2</sup>Carl von Ossietzky Universität Oldenburg, School of Mathematics and Science, Institute of Physics, 26129 Oldenburg, Germany

<sup>&</sup>lt;sup>3</sup>ForWind – Center for Wind Energy Research, Küpkersweg 70, 26129 Oldenburg, Germany

#### 1. Introduction

To meet growing electricity demand whilst reducing greenhouse gas emissions, the share of wind energy in the global energy mix is increasing rapidly, driven by the deployment of ever-larger wind turbines clustered into increasingly dense wind farms. When a turbine extracts energy from the wind, it generates a turbulent wake – a flow region of reduced velocity and elevated turbulence relative to the free stream. Owing to the regular arrangement of turbines in wind farms, most turbines operate within the wakes of upstream counterparts and thus experience (i) reduced available power (Kirby et al. 2025) and (ii) elevated incoming turbulence, which increases structural loads and accelerates fatigue damage (Thomsen & Sørensen 1999). Optimising wind farm layouts and turbine spacing to maximise power output and minimise maintenance therefore requires a thorough understanding of wind turbine wake evolution. Historically, studies on turbulent wakes have focused on the wakes of simple bluff bodies (cylinders, discs, spheres) developing in laminar or weakly turbulent inflows. Wind turbine wakes, however, evolve within a complex turbulent environment and exhibit far more intricate, multiscale dynamics than these canonical flows.

First, wind turbines consist of several bodies of varying sizes (blades, hub, nacelle, tower), resulting in wakes with multiple coherent structures – tip and root vortices, tower and nacelle vortex shedding, wake meandering – each characterised by distinct spatial and temporal scales (Vermeer, Sørensen & Crespo 2003; Porté-Agel *et al.* 2019). All statistics, dynamics and, ultimately, the structure of the near wake – typically extending 2D–4D downstream of the turbine (where D is the rotor diameter) – are strongly modulated by the rotor's geometry and operating conditions, such as the tip-speed ratio  $\Lambda$ , and the thrust coefficient  $C_T$  (Dong *et al.* 2023; Vahidi & Porté-Agel 2025). Further downstream, the far wake exhibits more universal behaviour as the influence of rotor-specific features diminishes: the mean velocity profile approaches a Gaussian distribution, tip vortices have largely decayed and wake meandering becomes the dominant dynamic feature (Bastankhah & Porté-Agel 2014; Yang & Sotiropoulos 2019). In this region, a single global turbine parameter, such as  $C_T$ , is generally assumed to be sufficient to integrate the overall effect of the turbine on the flow.

Second, both turbines and their wakes are exposed to complex turbulent environments, resulting from multiple interactions between the atmospheric boundary layer (ABL), the merging and mixing of turbulent wakes from upstream turbines and the developing internal wind farm boundary layer (Stevens & Meneveau 2017). Wind turbines operate within the lowest portion of the ABL, which contains a wide range of turbulence length scales,  $\mathcal{L}$  – from the Kolmogorov scale (O(mm)) up to a few kilometres – and varying freestream turbulence intensities,  $TI_{\infty}$ , with levels between 2 % and 15 % reported for offshore and onshore sites (Peña et al. 2016; Argyle et al. 2018). Moreover, wind turbine wakes exhibit elevated turbulence intensity levels that can persist over considerable distances, especially under low- $II_{\infty}$  inflow conditions. As rotor diameters grow and attractive wind farm sites like the North Sea become crowded, turbines are placed closer together, leading to higher wake-induced turbulence for downstream units. Understanding the influence of free-stream turbulence (FST) on wind turbine wake recovery is therefore critical, as it modulates the flow conditions experienced by downstream turbines – particularly the available kinetic energy they can extract – and ultimately affects the overall efficiency of a wind farm (Cal et al. 2010).

Typically, increasing FST intensity has been shown to accelerate wind turbine wake recovery, leading to a more rapid transition of the mean velocity profiles towards self-similarity, a faster reduction in the maximum velocity deficit, greater wake widths and increased wake expansion rates (Chamorro & Porté-Agel 2009; Chamorro et al. 2012b;

Rockel et al. 2017; Gambuzza & Ganapathisubramani 2023; van der Deijl et al. 2024). High- $I_{\infty}$  inflows enhance mixing between the low-momentum near-wake flow and the free stream, and importantly, accelerate the breakdown of tip vortices, which limit the exchange of mass, momentum and energy in the near field (Chamorro & Porté-Agel 2009; Lignarolo et al. 2014; Zhou et al. 2016). Although the influence of  $TI_{\infty}$  on wind turbine wakes is well documented – albeit primarily in the near field  $(x/D \lesssim 10)$  – the role of the FST integral length scale (ILS) remains far less explored, particularly experimentally. Generating turbulent inflows with ILS several times larger than the turbine diameter, as in the ABL, is experimentally challenging – especially when sufficiently high Reynolds numbers are required to achieve reasonable similarity to full-scale turbine wake physics, which often involves using turbine models with rotor diameters of  $O(10^{-1}-1 \text{ m})$ . Consequently, much of the current understanding of ILS effects on wind turbine wakes relies on largeeddy simulations (LES), which collectively show that the inflow turbulence ILS plays a key role in the wake recovery and dynamics. Several studies report that a larger ILS enhances wake recovery, promotes earlier onset of the velocity deficit reduction and produces wider wakes, while also amplifying wake meandering (Blackmore, Batten & Bahaj 2014; Du et al. 2021; Li et al. 2024; Vahidi & Porté-Agel 2024). Li et al. (2024) further reported that FST intensity and ILS accelerate the dissipation of the turbine-added turbulence kinetic energy (TKE), with the initial wake-added TKE increasing with ILS but decreasing with higher  $TI_{\infty}$ . In contrast, Hodgson et al. (2022, 2023) observed that inflows with shorter turbulence time scales enhance mixing and hasten wake recovery, notably through faster tipvortex breakdown; however, consistent with the other studies, they also report that longer time scales increase wake meandering. Overall, these LES results highlight the importance of accurately reproducing FST time and length scales in wind tunnel experiments.

In this context, recent advances in active turbulence-generating grids have enabled the experimental generation of inflows with turbulence length scales relevant to wind turbine applications (Hearst & Ganapathisubramani 2017; Neuhaus *et al.* 2020). Gambuzza & Ganapathisubramani (2023) investigated wind turbine wakes subjected to turbulent inflows with varying spectral contents and integral time scales generated using an active grid. Inflows with long turbulence time scales (up to 10 times the convective time scale) were classified as non-Kolmogorov-like flows due to the presence of a gap in the turbulence spectra. This gap results from the artificial forcing of low frequencies through grid motion. In contrast, inflows with shorter time scales and a canonical Kolmogorov spectrum were classified as Kolmogorov-like flows. For equal  $TI_{\infty}$ , wakes exposed to inflows with longer turbulence time scales recovered more slowly, whereas shorter time scales triggered earlier wake recovery – in agreement with the LES of Hodgson *et al.* (2022, 2023). However, it is difficult to ascertain whether this behaviour results solely from turbulence time-scale differences or also from deviations from a Kolmogorov-like energy distribution in the free-stream turbulence spectrum.

Importantly, recent experimental investigations into the effects of FST on the wakes of solid and porous bodies – porous discs being widely used as wind turbine surrogates in wind tunnel experiments – have revealed more intricate wake–FST interactions than those typically reported for turbine wakes. In the near wake of a cylinder ( $x/D \lesssim 10$ ), Buxton & Chen (2023), Kankanwadi & Buxton (2023), Chen & Buxton (2023, 2024) showed that both FST intensity and ILS enhance the entrainment of mass, momentum and kinetic energy relative to a non-turbulent background, thereby accelerating wake spreading and recovery. In contrast, in the far wake ( $x/D \gtrsim 30$ ), entrainment velocities and fluxes were observed to decrease with increasing FST intensity, with ILS exerting negligible influence (Kankanwadi & Buxton 2020; Chen & Buxton 2023, 2024). Comparable entrainment behaviour has been observed experimentally in porous-disc wakes: Vinnes *et al.* (2023),

Bourhis & Buxton (2024) reported reduced wake growth and entrainment rates for  $x/D \gtrsim 10$  at higher FST intensities, resulting in wider wakes in the far field under low-turbulence conditions (above a certain  $C_T$ ). Consistent numerical evidence was provided by Li *et al.* (2024) who reported smaller wake expansion rates at  $TI_{\infty} = 10$  % than at  $TI_{\infty} = 2.5$  % in their LES of permeable disc wakes, further reinforcing the picture of entrainment suppression in the far field at elevated FST intensities. In addition, Chen & Buxton (2023, 2024) identified a 'turning point' in cylinder wakes near  $x/D \approx 15$ , beyond which the wake grows at a markedly slower rate in both turbulent and non-turbulent background flows. Upstream of this location, FST intensity had minimal effect on entrainment velocities, whereas downstream, a clear reduction was observed with increasing  $TI_{\infty}$ .

Overall, these studies demonstrate that both FST intensity and ILS have a strong influence on bluff- and porous-body wakes, with effects that vary between the near and far field and with the thrust coefficient. These findings challenge the current understanding of wind turbine wakes, as there is no clear physical basis for the influence of FST to differ qualitatively from that observed in bluff- and porous-body wakes in the far field. A likely explanation lies in the restricted streamwise extent of most wind tunnel measurements – generally limited to less than 10D, matching typical turbine–turbine spacing in wind farms – whereas bluff- and porous-body wakes are examined over much greater distances. It is therefore plausible that wind turbine wakes have not been measured far enough downstream to reveal FST effects analogous to those reported in bluff- and porous-body far wakes. Extending wind turbine wake measurements into the far field could uncover a more universal entrainment behaviour.

In summary, while fundamental to wind farm optimisation, the combined effects of  $TI_{\infty}$ ,  $\mathcal{L}$  and  $C_T$  on wind turbine wakes remain insufficiently understood. The exploration of the  $\{C_T, TI_{\infty}, \mathcal{L}\}$  parameter space for a single turbine is relatively limited within individual studies, and cross-study comparisons can be challenging due to the lack of standardised turbine models and consistent experimental conditions. Variations in turbine geometry, operating parameters (e.g.  $C_T$ ,  $\Lambda$ ), and FST conditions (e.g. Reynolds number,  $\{TI_{\infty}, \mathcal{L}\}\$  combinations, turbulent energy spectral distribution) contribute to the dispersed and sometimes conflicting conclusions reported. To address this gap, we conducted an extensive parametric study of wind turbine wakes in high Reynolds number flows  $(Re > 10^5)$ , systematically examining the influence of the turbine thrust coefficient and FST conditions on the wake characteristics over streamwise distances of up to 20 turbine diameters. Specifically, the influence of 8 tailored FST 'flavours'  $\{TI_{\infty}, \mathcal{L}\}$  on the wake behind a single turbine operating at 3 different  $C_T$  is assessed, resulting in the evaluation of 24 different wind turbine wakes in the  $\{C_T, TI_{\infty}, \mathcal{L}\}$  parameter space. The remainder of the paper is structured as follows. The experimental set-up and the different  $\{C_T, TI_{\infty},$  $\mathcal{L}$  combinations are detailed in § 2. Section 3 analyses the influence of  $\{C_T, TI_{\infty}, \mathcal{L}\}$  on time-averaged turbulence statistics (§ 3.1), wake widths and growth rates (§ 3.2), wakeaveraged quantities ( $\S$  3.3), near-wake dynamics ( $\S$  3.4) and wake meandering ( $\S$  3.5). The key outcomes of this work are summarised in § 4.

#### 2. Experimental method

#### 2.1. Facility and experimental set-up

The experiments were performed in the  $3 \text{ m} \times 3 \text{ m} \times 30 \text{ m}$  test section of the large closed-loop wind tunnel at the University of Oldenburg. The outlet of the contraction nozzle is equipped with an active turbulence-generating grid, allowing the generation of customised turbulent inflow conditions (Neuhaus *et al.* 2020). The grid has 80 individually

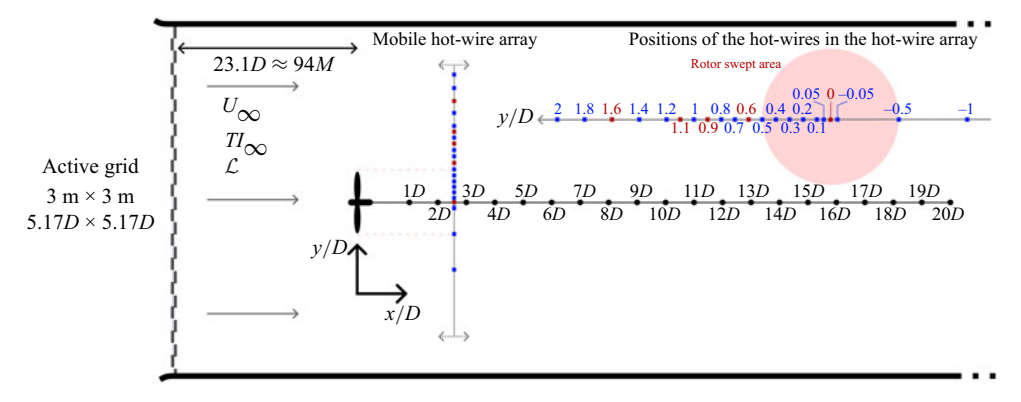


Figure 1. Schematic of the experimental set-up highlighting the positions of the hot-wires. Blue squares indicate hot-wires sampled at 6 kHz, while red squares represent hot-wires sampled at 20 kHz.

controllable shafts with rhombic aluminium wings mounted on them, resulting in a mesh width of M = 0.143 m. The grid blockage of the flow was altered by changing the angle of the wings  $\alpha(t)$ , i.e. the shaft angles, either dynamically (dynamic grid protocols) or statically (static grid protocols), with the latter resulting in a passive turbulencegenerating grid. In dynamic protocols, the local grid blockage was varied over time based on predefined shaft-angle time series, while the global blockage, computed over the entire grid, remained constant at every instant. Further details on the transfer functions linking grid protocols to the resulting flows can be found in Neuhaus et al. (2021). The specific grid excitation protocols used in this study, along with the corresponding dynamics of the generated turbulence, will be presented in § 2.2. The wind turbine used was the Model Wind Turbine Oldenburg 0.6 (D = 0.58 m, three blades, tower height 0.45 m). The turbine was positioned  $23.1D \approx 94M$  downstream of the active grid and mounted on a platform such that the hub centre was 0.96 m above the wind tunnel floor. The origin of the coordinate system is at the intersection between the rotation axis and the plane formed by the blades' leading edges. The thrust (T) acting on the turbine was measured using strain gauges mounted on the tower and set in a full bridge configuration. The wind turbine was maintained at a constant tip-speed ratio ( $\Lambda = D\omega/2U_{\infty}$ , where  $\omega$  is the rotor angular velocity) and thrust coefficient  $(C_T = T/0.5\rho\pi(D/2)^2U_{\infty}^2)$ , where  $\rho$  is the air density) during the tests using a real-time closed-loop load control. The turbine was operated at three thrust coefficients  $-C_T \in \{0.5, 0.7, 0.9\}$  – corresponding to tip-speed ratios of  $\Lambda \in \{1.7, 2.7, 3.7\}$ . We will refer to these operating points as low-, medium- and high- $C_T$ in the text. Because the blade pitch angle is the same for all cases, changing  $C_T$  necessarily changes  $\Lambda$ , making it impossible to isolate their individual effects on the wakes. The incoming wind speed was  $U_{\infty} \approx 6.5 \text{ m s}^{-1}$  for all FST cases, resulting in a diameter-based Reynolds number of  $Re \approx 2.55 \times 10^5$ . Although this global Reynolds number is lower than those typically experienced by large-scale wind turbines  $(Re \sim 10^6 - 10^7)$ , which could lead to some differences in instantaneous flow characteristics (Bourhis, Pereira & Ravelet 2023), Chamorro et al. (2012a) showed that above  $Re \approx 9.4 \times 10^4$ , the main flow statistics (mean velocity, turbulence intensity, kinematic shear stress and velocity skewness) become Reynolds number independent.

A motorised array consisting of 21 single hot-wire probes was used to horizontally scan the wake at hub height (z = 0) for  $x/D \in [1, 20]$  in steps of 1D. The positions of the hot-wires are highlighted in figure 1. Half of the wake was scanned with high spatial resolution, while the other half was scanned sparsely and primarily used to ensure turbine alignment and wake symmetry. Previous full-wake scans using identical experimental set-ups have

Case	Protocol	$\overline{\alpha}$ (°)	$\sigma_{\alpha}$ (°)	$\Omega$ (°s <sup>-1</sup> )	$TI_{\infty}$ (%)	$\mathcal{L}_x/D$	$\mathcal{L}_{ extit{y}}\!/\!D$	$\mathcal{L}_x/\mathcal{L}_y$
S1 +	Static	$0^{\circ}$	$0^{\circ}$		$0.9 \pm 0.1$	$0.09 \pm 0.01$	$0.13 \pm 0.01$	0.7
$S2 \times$	Static	30°	$0^{\circ}$	_	$1.8 \pm 0.1$	$0.16 \pm 0.01$	$0.15 \pm 0.01$	0.9
S4 •	Static	$0^{\circ} - 90^{\circ}$	$0^{\circ}$	_	$4.5 \pm 0.4$	$0.34 \pm 0.04$	$0.23 \pm 0.01$	1.5
M5 ■	Dynamic	30°	10°	$152^{\circ}  \mathrm{s}^{-1}$	$4.9 \pm 0.3$	$1.17 \pm 0.26$	$0.72 \pm 0.06$	1.6
L3 ▼	Dynamic	30°	$2.5^{\circ}$	$10^{\circ}  \mathrm{s}^{-1}$	$3.7 \pm 0.3$	$1.76 \pm 0.17$	$1.09 \pm 0.10$	1.6
L6 🔷	Dynamic	30°	5°	$20^{\circ}  \mathrm{s}^{-1}$	$5.8 \pm 0.4$	$1.95 \pm 0.20$	$1.09 \pm 0.10$	1.8
L7 🍸	Dynamic	30°	10°	$39^{\circ}  \mathrm{s}^{-1}$	$8.8 \pm 0.4$	$1.93 \pm 0.27$	$0.93 \pm 0.05$	2.1
L8 🙏	Dynamic	30°	15°	$61^{\circ}  \mathrm{s}^{-1}$	$10.8 \pm 0.5$	$2.00 \pm 0.29$	$0.90 \pm 0.04$	2.2

Table 1. Active grid operating parameters and corresponding FST characteristics for the 8 turbulent inflows.

confirmed the symmetry of the wake (Hulsman et al. 2022; Messmer, Hölling & Peinke 2024), thereby justifying half-wake measurements. Three hot-wires were positioned in close proximity around y = 0 to capture the wake centreline with the highest possible spatial resolution, while the density of the hot-wires decreases progressively from the geometric centreline to the edge of the wind tunnel. Five hot-wires were operated at  $f_s = 20 \,\mathrm{kHz}$  using a StreamLine Pro CTA system 9091N0102 with 91C10 CTA (constant temperature anemometer) modules from Dantec Dynamics (hot-wires highlighted in red in figure 1). All remaining probes were operated with multichannel 54N80 CTA modules and sampled at  $f_s = 6 \,\text{kHz}$ . Both systems were synchronised and data were acquired for 240 s at each streamwise position, which is sufficiently long to ensure the convergence of all the quantities introduced and discussed in this paper. The hot-wires were calibrated twice daily. Differential pressure was measured using a Prandtl tube, and air density was computed based on the measured temperature, atmospheric pressure and humidity. The hot-wire voltages were then converted into velocity using a fourth-order polynomial law. For each individual measurement point, the acquisition time was compared with the times at which the two calibrations were performed to compute a weighted average calibration, which was then used to convert the voltage signal to velocity. For each velocity profile, the mean of the time-averaged velocities measured by the two farthest hot-wires  $(y/D \in \{1.8, 2\})$  was used as the normalising measurement to account for the minor variations in the free-stream velocity along the length of the tunnel (less than 4 % over the entire measurement region for all cases).

#### 2.2. Free-stream turbulence 'flavours'

Eight different FST 'flavours' were generated using static and dynamic grid protocols. The first five columns of table 1 show the active grid operating parameters for the different FST cases. Images and movies showing the active grid in operation are available in the https://doi.org/10.1017/jfm.2025.10788. With the exception of case S1, for which the grid was fully open ( $\alpha=0^{\circ}$ ), the overall blockage of the grid to the flow remained the same for all FST cases. Here,  $\alpha$  is the angle of the wings relative to the incoming wind and is directly linked to the grid blockage. In case S4, the wings alternated between being fully open and fully closed ( $\alpha=90^{\circ}$ ), mimicking a regular grid pattern. In case S2, the wings were set to a constant angle  $\alpha=30^{\circ}$  along either the  $\pm y$ -axis or the  $\pm z$ -axis, ensuring a symmetrical distribution to prevent deflecting the flow towards any particular side of the wind tunnel. Finally, in protocols M5, L3, L6, L7 and L8, the instantaneous local blockage was varied dynamically, with the angle standard deviation,  $\sigma_{\alpha}$ , and the angular speed of the wings  $\Omega$  differing across the protocols. Here,  $\Omega=|\dot{\alpha}|$  denotes the time-averaged absolute

rotational rate of the grid's flapping wings, which oscillate back and forth around the mean angle  $\overline{\alpha}$  during a dynamic protocol, without completing a full rotation, unlike in classical double random mode protocols. However, at each instant, the global blockage, computed across the entire grid, remained identical across all protocols (both static and dynamic), so that the time-averaged angle over a grid cycle was similar ( $\overline{\alpha}=30^\circ$ , along the  $\pm y$ -axis or  $\pm z$ -axis). The hot-wire acquisition system was synchronised with the grid protocol to ensure that data recording at each streamwise measurement station began at the start of a repeated grid cycle, thereby maintaining consistent inflow conditions across all stations. Each grid cycle lasted 5 min, providing sufficient time for the 4 min hot-wire measurements and for the hot-wire cart to move between stations.

To characterise the turbulent inflows, the test section was left empty and the hotwires were evenly spaced across the width of the wind tunnel (in the range  $-1.4 \,\mathrm{m} \le$  $y \le 1.4$  m). The horizontal hot-wire line was positioned at z/D = z/D = 0, i.e. within the turbine's swept plane. In this paper, the velocity is decomposed using the Reynolds decomposition as  $U(x, y, t) = \overline{U}(x, y) + u'(x, y, t)$ , with the overline  $\overline{\cdot}$  denoting a temporal average, and the brackets (•) denoting a spatial average along the horizontal axis y. The various turbulent background flows were characterised in terms of FST intensity,  $TI_{\infty} = \sqrt{\overline{u'^2}}/U_{\infty}$ , and ILSs,  $\mathcal{L}_x$  and  $\mathcal{L}_y$ . The streamwise ILS,  $\mathcal{L}_x$ , provides an estimation of the turbulence length scale along the main flow direction, while the spanwise ILS,  $\mathcal{L}_{v}$ , describes the lateral extent of the incoming flow coherent structures.  $\mathcal{L}_{x}$ is determined from the prior estimation of the integral time scale  $\mathcal{T} = \int_0^{\tau_0} R'(\tau) d\tau$ , and by assuming Taylor's hypothesis  $\mathcal{L}_x = U_{\infty} \mathcal{T}$ . Here,  $R'(\tau)$  is the temporal correlation between u'(x, y, t) and  $u'(x, y, t + \tau)$  integrated up to  $\tau_0$ , where  $R'(\tau_0) = 0.1$ . Similarly,  $\mathcal{L}_y =$  $\int_0^{r_0} R'(r) dr$  is computed by integrating the spatial correlation R'(r) between u'(x, y, t)and u'(x, y + r, t). Since the hot-wires were linearly spaced along the tunnel width, the spatial resolution for the integration dr is limited to the distance between each hot-wire, which is 14 cm. Moreover, for the hot-wires located near the walls, the range of r for performing the correlation is maximal (e.g. 2.8 m for the probe closest to the wall, covering almost the entire width of the wind tunnel). This allows for the integration of R'(r) up to the first zero crossing  $(R'(r_0) = 0)$  in all FST cases, particularly those characterised by a large spanwise ILS. In contrast, for the hot-wires located in the central region, the range of r is smaller (e.g. 1.4 m for the centreline probe) such that for large ILS inflows, the correlation function R'(r) does not reach zero. Hence, for the sake of consistency, the integration is performed up to  $r_0$ , where  $R'(r_0) = 0.1$  for all FST cases. Profiles of  $TI_{\infty}$ ,  $\mathcal{L}_x$  and  $\mathcal{L}_y$  for all FST cases are shown in Appendix A, along with plots of the temporal,  $R'(\tau)$ , and spatial, R'(r), correlation functions for selected FST cases and hotwires. The decay of the FST intensity along the measurement region was assessed and found to be minimal across all cases. The largest decay was observed for the highest- $TI_{\infty}$  case, L8, with  $TI_{\infty}(x/D=0) - TI_{\infty}(x/D=20) \approx 2\%$ . The experimental envelopes of the 8 different turbulent inflows are obtained by averaging the profiles of  $TI_{\infty}$ ,  $\mathcal{L}_x$ and  $\mathcal{L}_{y}$  for  $y(m) \in [-1.2, 1.2]$  (i.e.  $y/D \in [-2.1, 2.1]$ ). The last four columns of table 1 present the averaged quantities and their respective standard deviation, while a graphical representation of the different FST 'flavours',  $\{TI_{\infty}, \mathcal{L}_{x,y}\}$ , is provided in figure 2.

A specific nomenclature is established to classify the FST cases, denoted as 'case ##' (e.g. case S1). The letter (S, M, L) specifies the turbulence ILS – small (S1, S2, S4), medium (M5) or large (L3, L6, L7, L8) – while the number (1–8) indicates the inflow turbulence intensity,  $TI_{\infty}$ , ranked in hierarchical order from lowest (#1) to highest (#8). For clarity, the cases are also grouped by FST intensity into group 1 (low- $TI_{\infty}$ ), group 2 (medium- $TI_{\infty}$ ) and group 3 (high- $TI_{\infty}$ ). The FST parameter space encompasses a broad

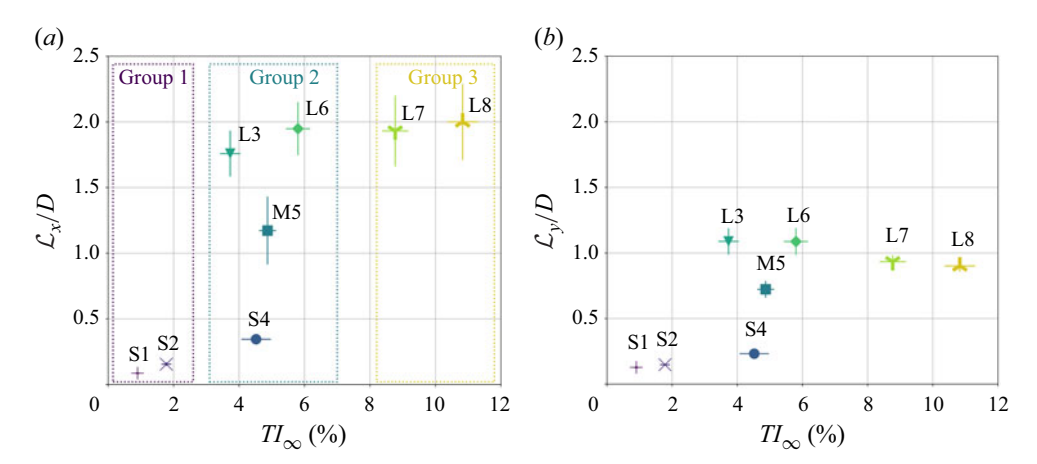


Figure 2. Experimental envelope of FST characteristics for the 8 inflows.

range of FST intensities (1 %  $\lesssim TI_{\infty} \lesssim$  11 %) and streamwise ILSs (0.1  $\lesssim \mathcal{L}_x/D \lesssim$  2), representative of inflow conditions typically experienced by full-scale wind turbines (Argyle et al. 2018; Burton et al. 2021). Low turbulence levels are characteristic of offshore wind sites, whereas higher levels are typical within wind farms or at onshore locations. The FST intensities considered here fall within the turbulence classes defined in the IEC 61 400-1 standard, which specifies wind turbine design and safety requirements based on site-specific wind conditions (IEC 2019). Figure 2 shows that  $\mathcal{L}_x > \mathcal{L}_y$ , highlighting the streamwise stretching of the turbulent structures, while  $\mathcal{L}_{v}$  remains smaller than the tunnel width, thereby supporting the validity of the estimation method. Although the inflow ILS-to-diameter ratios are smaller than in the ABL, the FST cases span well-separated characteristic scales:  $\mathcal{L}_x < D/2$  for cases S#,  $\mathcal{L}_x \simeq D$  for case M5, and  $\mathcal{L}_x \simeq 2D$  for cases L#. In addition, the inflow  $\{TI_{\infty}, \mathcal{L}_x\}$  parameter space is expected to help distinguish the respective influences of FST intensity and ILS on turbine wake recovery. Comparisons among cases L# may allow us to isolate the role of  $TI_{\infty}$ , as their  $\mathcal{L}_x$  are nearly identical, while cases S# enable a similar comparison but at smaller ILS. Finally, comparisons within group 2 are likely to emphasise the influence of ILS, since variations in  $\mathcal{L}_x$  are a priori more pronounced than those in  $TI_{\infty}$ .

The power spectra of all FST cases exhibit a -5/3 slope with no gap in the energy cascade between large and small scales, even for cases L# with the largest ILS (Appendix A); this confirms that the inflow turbulence is fully developed at the turbine location. All turbulent inflows are therefore Kolmogorov-like flows as defined by Gambuzza & Ganapathisubramani (2023), with the L# cases exhibiting large inertial subranges (around 2 decades). Finally,  $\{C_T, \Lambda\}$  for all inflow conditions are reported in Appendix B, where it can be observed that neither parameter is significantly affected by variations in FST intensity or ILS.

#### 3. Results

## 3.1. Profiles of turbulence statistics

## 3.1.1. Time-averaged velocity deficit

The time-averaged velocity deficit profiles  $(\Delta U/U_{\infty})$ , where  $\Delta U = U_{\infty}(x) - \overline{U}(x, y)$  at five streamwise locations are presented in figure 3 for FST cases S1, S4, M5, L6 and L8. At the nearest location (x/D = 1), the profiles are nearly identical across all FST cases within

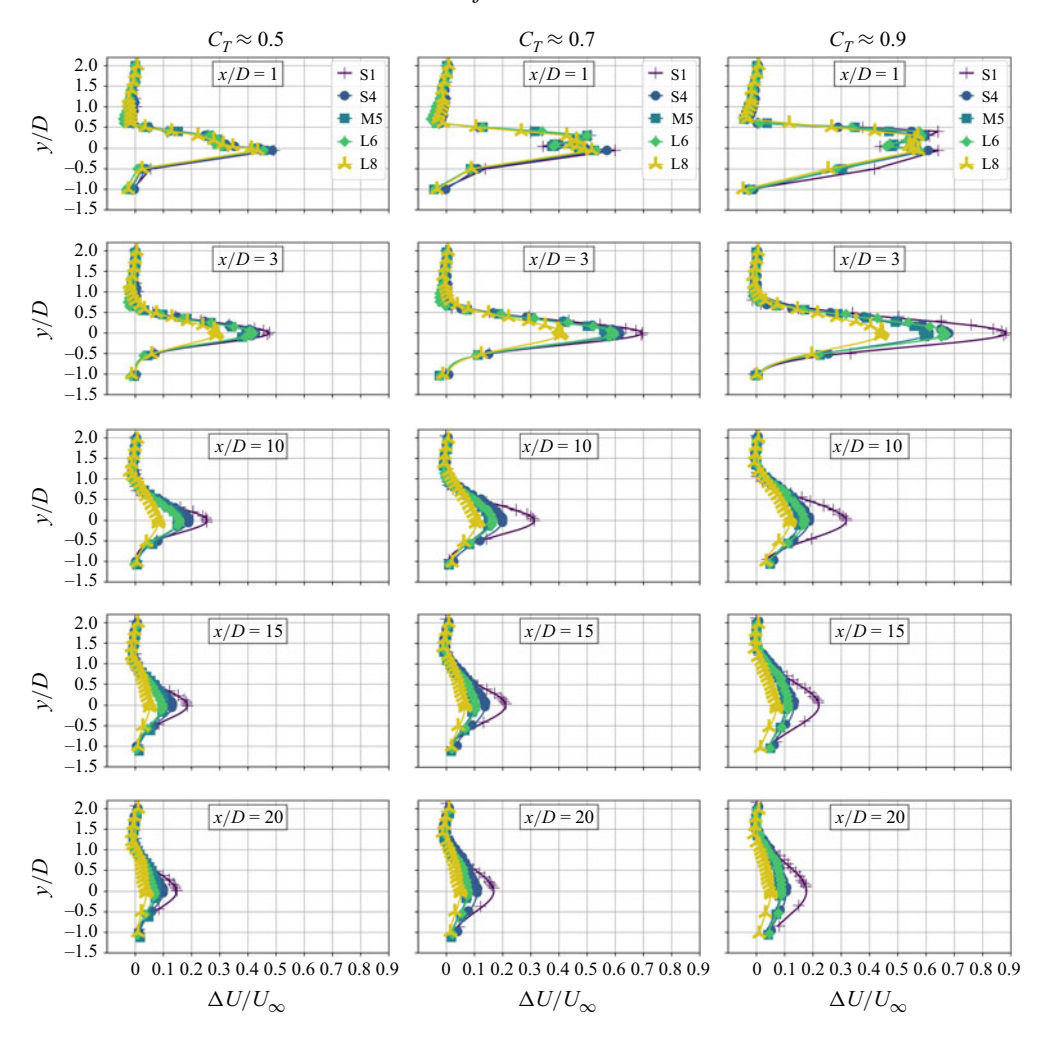


Figure 3. Time-averaged velocity deficit profiles.

each  $C_T$  group, as expected from momentum theory  $(C_T \sim \int \overline{U} \Delta U r dr)$ . As the wakes develop, the velocity deficit profiles gradually evolve towards a Gaussian-like distribution – consistent with the far-wake shape typically assumed in engineering wake models (e.g. Bastankhah & Porté-Agel 2014) – with higher  $TI_{\infty}$  accelerating this transition. Although slight deviations from an ideal Gaussian shape remain near the wake edge, within the shear layer where tip vortices may persist, the profiles for  $x/D \geqslant 3$  closely follow a Gaussian-like distribution for all  $\{C_T, FST\}$  combinations.

Considering FST effects, clear differences in both the magnitude and width of the velocity deficit profiles are observed for all  $C_T$  after only a few diameters, highlighting the strong and immediate impact of FST. While a detailed analysis of wake velocity recovery is provided in § 3.3, it is already evident that both FST intensity and ILS affect the recovery of the maximum velocity deficit,  $(\Delta U/U_{\infty})_{max}$ , with differences between FST cases becoming more pronounced as  $C_T$  increases. Relative to the closest approximation of a non-turbulent inflow (case S1), the presence of FST generally accelerates the reduction of  $(\Delta U/U_{\infty})_{max}$ . However,  $(\Delta U/U_{\infty})_{max}$  does not decrease monotonically with increasing FST intensity because of the concurrent effect of the ILS. For instance,  $(\Delta U/U_{\infty})_{max,L6} \ge$ 

 $(\Delta U/U_{\infty})_{max,M5}$  across the entire measurement domain for  $C_T \in \{0.7, 0.9\}$  and up to  $\sim 10D$  for  $C_T = 0.5$ , clearly showing that, for similar FST intensities, a larger turbulence ILS leads to a slower recovery of the maximum velocity deficit.

In the far field  $(x/D \gtrsim 15)$ , the presence of a strong turbulent background appears to interfere with the wake's Gaussian structure – particularly for  $C_T \approx 0.5$  (e.g. see the L8 profiles at  $x/D \geqslant 15$ ). The relatively weak momentum deficit remaining in this region, compared with the strength of the background turbulence, may be insufficient to 'sustain' a Gaussian distribution, with strong turbulent events potentially disrupting a self-similar evolution of the wake (Rind & Castro 2012). At the farthest measurement station (x/D = 20), a residual velocity deficit profile is still measurable for all  $\{C_T, FST\}$  combinations, emphasising the considerable distance needed for the mean velocity to fully recover.

In the lowest  $TI_{\infty}$  case (S1), the near-field differences in the width and magnitude of the  $\Delta U/U_{\infty}$  profiles, driven by variations in  $C_T$ , persist across the entire measurement range and remain clearly discernible even at x/D=20. As  $TI_{\infty}$  increases, however, these  $C_T$ -induced differences progressively diminish; by x/D=20, the variations in  $\Delta U/U_{\infty}$  between  $C_T$  cases are barely noticeable in high- $TI_{\infty}$  conditions. Thus, the presence of a strong turbulent background rapidly suppresses the influence of  $C_T$  on  $\Delta U/U_{\infty}$ , whereas in low FST intensity the wake retains a clear imprint of the operating point and a memory of its initial conditions far downstream.

# 3.1.2. Turbulence intensity and kinetic energy

The profiles of turbulence intensity  $(TI = \sqrt{u'^2}/\overline{U})$ , and turbine-added streamwise TKE  $(\Delta k = (k - k_\infty)/U_\infty^2)$  are shown in figures 4 and 5. To account for the slight streamwise decay of the background TKE, inherent to grid-generated turbulence,  $k_\infty$  is computed at each x-location as the average of the TKE measured by the two hot-wires farthest from the centreline, i.e.  $k_\infty(x) = \langle k(x, y/D = 1.8, 2) \rangle$ , with  $k = 0.5 \overline{u'^2}$ .

At the nearest location (x/D = 1), both TI and  $\Delta k$  in the wake increase with  $C_T$  and  $TI_{\infty}$  – in contrast to the LES results of Li et al. (2024) who reported a decrease in  $\Delta k$ with increasing  $TI_{\infty}$  – while the influence of the inflow ILS appears secondary. For all  $\{C_T, FST\}$  combinations, a peak of turbine-induced TKE is observed in the rotor tip shear layer, whose magnitude increases with both  $C_T$  and  $TI_{\infty}$ . As the wake develops, the tip shear layer expands inward and outward, resulting in a decrease in the TKE peak and an initial rise in the centreline TKE, which then gradually decays as the wake mixes with the ambient flow. A similar build-up of the centreline TI, fuelled notably by the highshear tip region, is also observed in the near field before the turbulence intensity begins to decay downstream. While the turbine-added TKE profiles for low- and medium- $II_{\infty}$  cases exhibit the characteristic saddle shape of self-similar axisymmetric wakes throughout the measurement domain, the presence of a strong turbulent background disrupts this structure (see case L8), mirroring the breakdown of self-similar Gaussian velocity deficit profiles. Interestingly, Rind & Castro (2012) reported a similar behaviour in the far field of a solid disc  $(x/D \ge 65)$ , showing that the presence of a sufficiently strong turbulent background  $(TI_{\infty} \ge 3.3\%$  in their experiments) suppresses the possibility of self-similarity in the far wake due to the substantial transformation of the wake's turbulence structure by the FST, whereas self-similar behaviour was observed for  $TI_{\infty} \leq 1.2$  %. This loss of self-similarity was particularly evident in the turbulence normal stresses, which deviated from their typical self-similar cross-stream behaviour (the saddle shape), gradually flattening across the radial axis and aligning with free-stream levels, as observed in our wind turbine wake experiments.

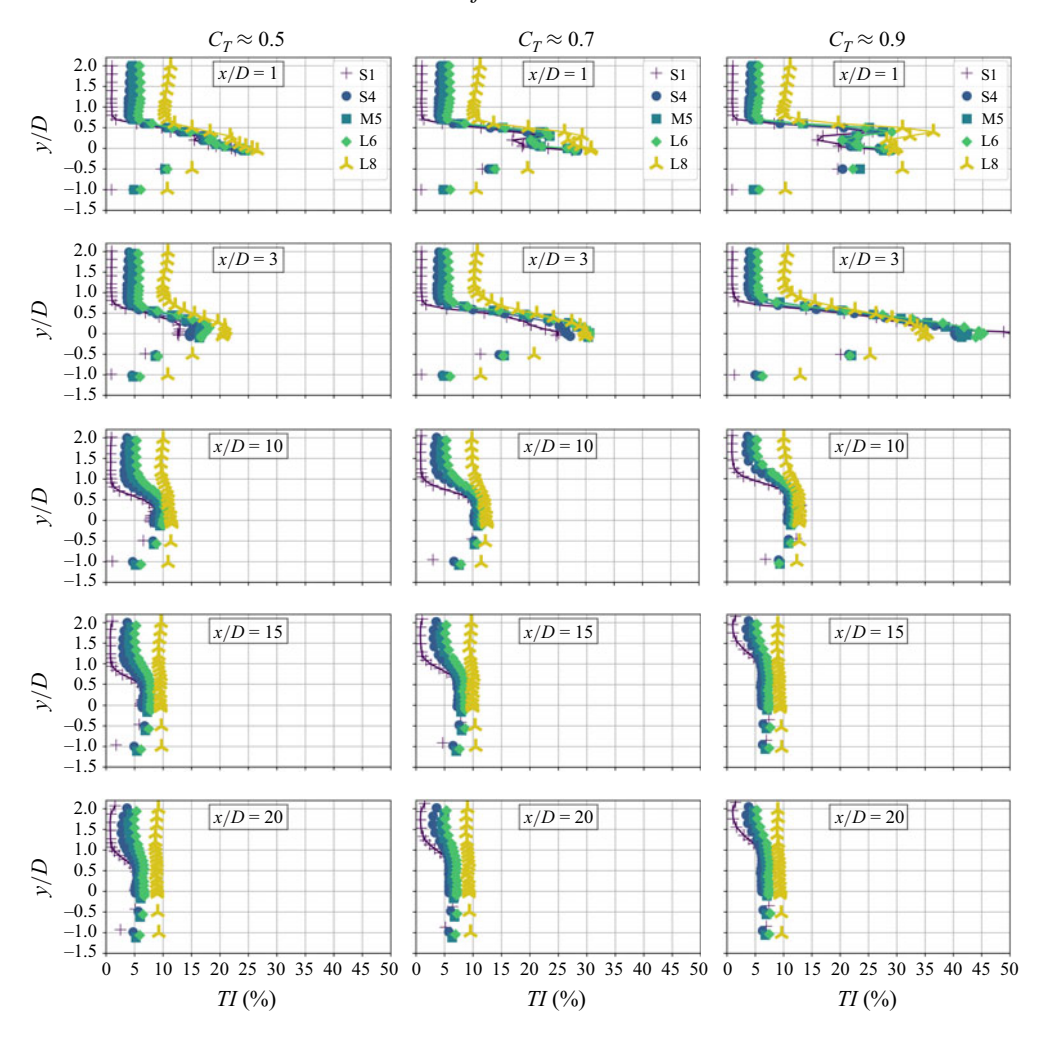


Figure 4. Turbulence intensity profiles.

The rate at which TI and  $\Delta k$  decay in the near field increases as both  $C_T$  and  $TI_{\infty}$  increase, consistent with findings on porous-disc wakes (Bourhis & Buxton 2024; Li *et al.* 2024). Near the turbine  $(x/D \leq 3)$ , the following trend is observed:  $\Delta k_{Group3(L8)} \geqslant \Delta k_{Group2(S4,M5,L6)} \geqslant \Delta k_{Group1(S1)}$ . However, this relationship reverses farther downstream  $(x/D \gtrsim 15)$ , where  $\Delta k_{L8} \leqslant \Delta k_{L6,M5,S4} \leqslant \Delta k_{S1}$ , indicating a faster mixing of the low-TKE background flow with the high-TKE wake as  $TI_{\infty}$  increases. The faster decay of TI and TKE in the near field as  $TI_{\infty}$  increases likely results from enhanced turbulence mixing due to both higher  $TI_{\infty}$  and an increased initial  $\Delta k$ . For group 2 cases (S4, M5 and L6), larger variations in  $\Delta k$  are observed in the near field  $(x/D \lesssim 5)$  than in the far field  $(x/D \gtrsim 15)$ , which may be attributed to differences in ILS. For instance, when comparing cases L6 and M5 at x/D = 3,  $\Delta k_{y=0,L6} < \Delta k_{y=0,M5}$  for all  $C_T$ , in contrast to the general trend of increasing  $\Delta k$  with higher  $TI_{\infty}$ , suggesting that a larger ILS may slow the dissipation of the turbine-added TKE.

At x/D=3, the turbulence intensity exhibits distinct behaviour depending on  $C_T$ : for  $C_T \in \{0.5, 0.7\}$ ,  $TI_{L8} \ge TI_{M5} \ge TI_{S4} \ge TI_{S1}$ , consistent with the increase in  $TI_{\infty}$  (figure 4). For  $C_T=0.9$ , however, the trend is reversed, with  $TI_{L8} \le TI_{M5,S4} \le TI_{S1}$ .

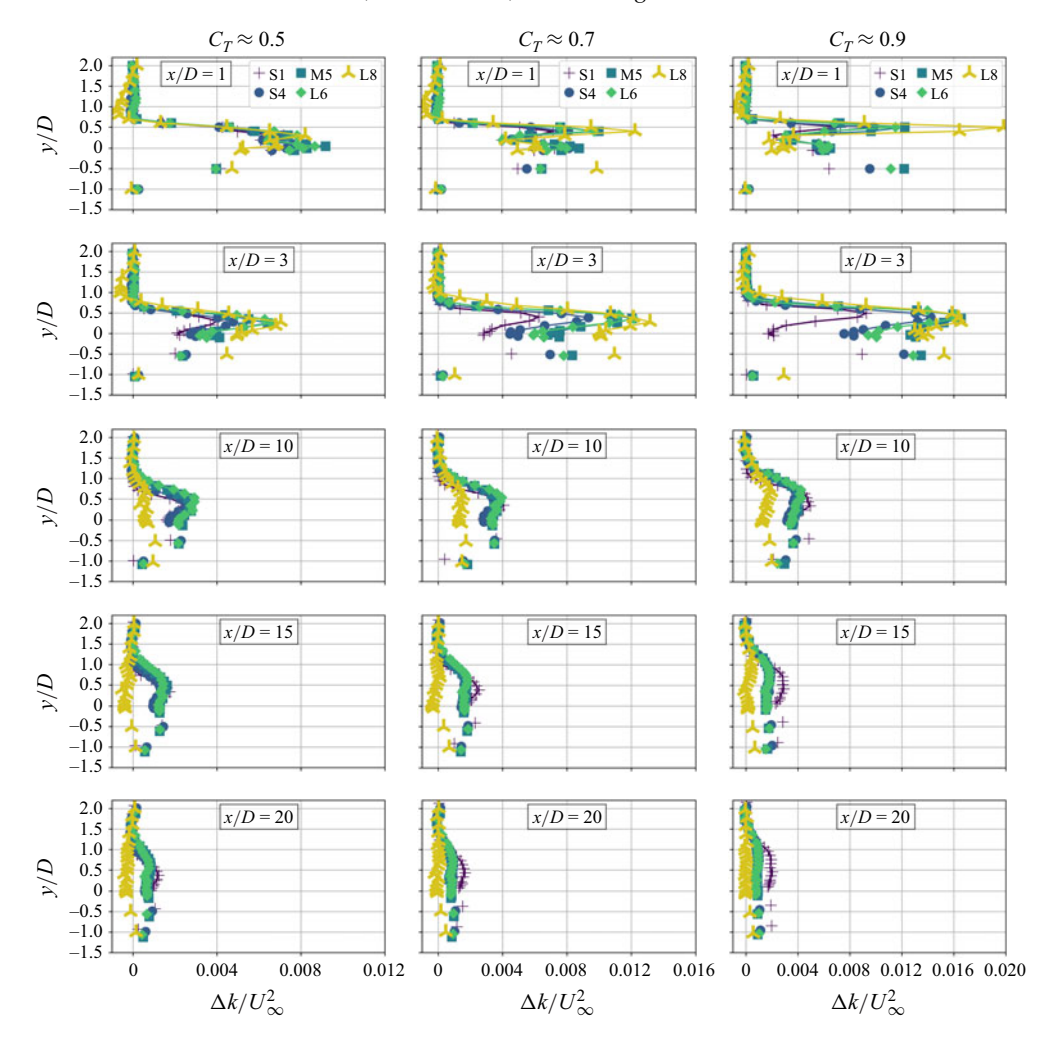


Figure 5. Turbine-added TKE profiles. Note the change in the abscissa scale across the different  $C_T$  cases.

This inversion is likely a consequence of the substantially higher wake TI levels at large  $C_T$ , which amplify the difference between the wake and background turbulence intensities, thereby enhancing wake mixing and accelerating the dissipation of TI in the near field. This rapid decay of TI in the near field is further intensified in high- $TI_{\infty}$  inflows. In the far field, wake TI levels gradually converge towards background levels, such that the cases with the highest  $TI_{\infty}$  also exhibit the largest TI within the wake. By definition, the decay rate of TI depends on both the mean velocity recovery and the dissipation of the TKE – processes that evolve at different rates – which explains why  $\Delta k$  and TI do not exhibit identical streamwise evolution.

Interestingly, in the highest  $TI_{\infty}$  case (L8), the wake turbulence intensity becomes nearly equal to the free-stream level ( $TI \approx TI_{\infty}$ ) beyond  $x/D \gtrsim 15$ , resulting in quasi-flat TI profiles in the far field for all  $C_T$  (figure 4). Similarly, the turbine-added TKE decays to  $\Delta k \approx 0$  (figure 5), consistent with the findings of Rind & Castro (2012). Thus, although a mean momentum deficit persists in the far field – evidenced by the small time-averaged velocity deficit at x/D = 20 – the far wake no longer exhibits elevated turbulence levels. The faster decay of  $\Delta k$  relative to  $\Delta U$  indicates that the background TKE is entrained and

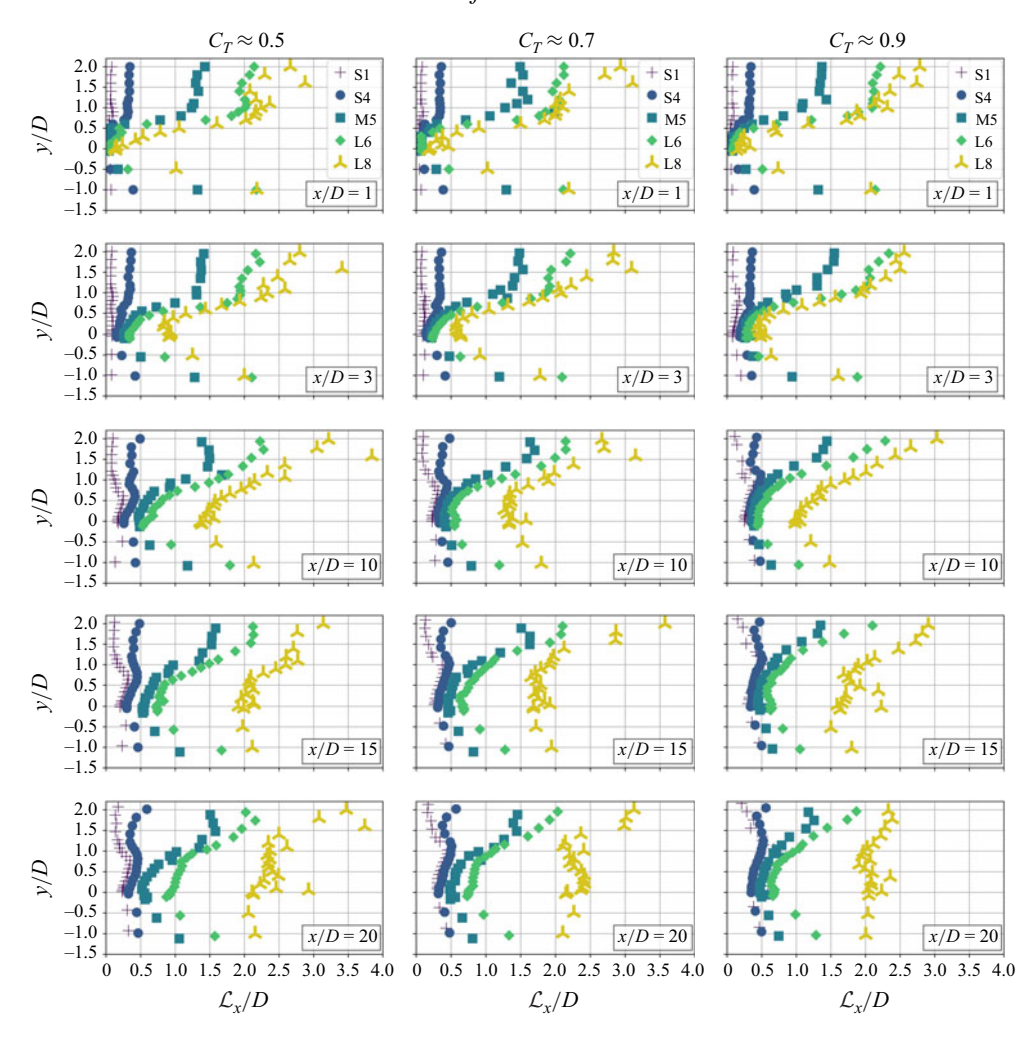


Figure 6. Streamwise turbulence ILS profiles.

mixed into the wake more efficiently than the momentum. This observation is consistent with the cylinder wake results of Buxton & Chen (2023), who found that the TKE is entrained more efficiently than both mass and momentum in the near field in the presence of FST. Consequently, it results in a scenario where the wind turbine far wake becomes a flow region distinct from the free stream solely by a reduced mean momentum, rather than by elevated turbulence levels. Zhang, Yang & He (2023) reported a comparable behaviour in their LES of wind turbine wakes under various ABL inflow conditions, identifying a far-field region ( $x/D \gtrsim 40$ ) where the turbine-added TKE had fully homogenised with that of the free stream despite a persisting momentum deficit. They further observed that the full dissipation of  $\Delta k$  occurred closer to the turbine as  $TI_{\infty}$  increased, aligning with our observations.

# 3.1.3. Turbulence integral length scale

Figure 6 shows the profiles of streamwise turbulence ILS,  $\mathcal{L}_x$ , for FST cases S1, S4, M5, L6 and L8. The turbulence ILS in the wake is computed in a similar manner to the background turbulence ILS, as  $\mathcal{L}_x = \overline{U} \int_0^{\tau_0} R'(\tau) d\tau$ , with  $R'(\tau_0) = 0.1$ . Although the application of

Taylor's frozen turbulence hypothesis in the near wake may introduce some additional uncertainty in estimating  $\mathcal{L}_x$ , the consistent evolution of the profiles from the near to far field across all wakes suggests that any error introduced by this assumption remains small.

Similar to the velocity deficit, an ILS 'deficit' is observed in the near field for all  $\{C_T, FST\}$  combinations, with  $\mathcal{L}_x(x/D=1)$  consistently smaller than the background ILS. The rotor acts as a high-pass filter, suppressing the largest scales of the incoming turbulence (Chamorro *et al.* 2012b). This effect is particularly pronounced for the M# and L# cases, whose ILS radial profiles exhibit steep gradients near the wake edge, whereas in the S# cases the profiles are nearly flat – although  $\mathcal{L}_x(x/D=1)$  remains slightly smaller than the background ILS. As both  $C_T$  and  $\Lambda$  increase, the streamtube within which large structures are filtered broadens radially, a trend further reflected in the wider ILS profiles observed at high  $C_T$ .

Interestingly, further downstream, the evolution of  $\mathcal{L}_x$  in the wakes depends strongly on the inflow ILS. For cases S#, the ILS in the wakes exceeds that of the inflows for  $x/D \gtrsim 3$ . In particular, the peak in  $\mathcal{L}_x$  around  $y/D \approx 0.6$  grows and shifts outward as the wake spreads, highlighting the progressive development of coherent structures in the tip shear layer. These structures grow with increasing x and  $C_T$ , with  $\mathcal{L}_{x,Low-C_T} \leqslant \mathcal{L}_{x,Med-C_T} \leqslant$  $\mathcal{L}_{x,High-C_T}$  throughout the measurement domain. A similar behaviour has been reported for porous-body wakes developing in a non-turbulent background: small vortices, initially confined to the tip shear layer, merge and form larger structures as the shear layer develops (Bourhis & Buxton 2024; Cicolin et al. 2024). It can be noted that shear-layer instability, analogous to vortex shedding in bluff-body wakes, is one of two mechanisms proposed for the onset of wake meandering (e.g. Yang & Sotiropoulos 2019). The other, which underpins the dynamic wake meandering (DWM) model (Larsen et al. 2008), hypothesises that wind turbine wakes are passively advected by large-scale free-stream eddies that drive their meandering motion. While this topic is discussed in more detail in § 3.5, it is worth noting here that, for small- $\mathcal{L}_x$  FST cases (S#), the largest wake structures originate in the tip shear layer, grow downstream and are influenced by the turbine thrust coefficient – and hence its porosity – sharing similarities with bluff-body shear-layer behaviour.

In contrast, for the M# and L# cases, the ILS within the wakes remains smaller than the background ILS, with no peak in  $\mathcal{L}_x$  in the tip shear layer – the rotor's high-pass filtering effect persists across the entire measurement domain. For these cases,  $\mathcal{L}_x$  in the wake gradually aligns with that of the free stream, akin to the recovery of the velocity deficit, with a larger background ILS promoting a faster recovery of  $\mathcal{L}_x$ . Unlike the S# cases,  $\mathcal{L}_{x,Low-C_T} \geqslant \mathcal{L}_{x,Med-C_T} \geqslant \mathcal{L}_{x,High-C_T}$  throughout the wake, indicating a faster recovery of  $\mathcal{L}_x$  at lower  $C_T$ . This behaviour can be qualitatively interpreted by analogy with porous discs: at higher porosity (lower  $C_T$ ), larger turbulence structures pass through the rotor without being filtered, leading to slightly larger  $\mathcal{L}_x$  in the near field and a faster recovery.

In summary, for cases S#, the large-scale wake structures are primarily turbine-induced, shear-layer-generated coherent structures whose evolution is strongly influenced by the turbine operating point. Structures originating in the tip shear layer grow and propagate towards the background flow, leading to an ILS within the wake that exceeds the inflow ILS. In contrast, for M# and L# FST cases, the ILS within the wake recovers similarly to TI and  $\Delta U$ , progressively increasing to adjust with that of the inflow turbulence, with larger background ILS promoting a faster adjustment of the ILS. Enhanced wake meandering, vortex-vortex interaction between the FST and the wake, or the entrainment of large eddies from the free stream could explain the progressive adjustment of the ILS. For the FST parameter space examined, distinct interactions between the background flow and the wake are observed depending on  $\mathcal{L}_x$ : for  $\mathcal{L}_x \lesssim 0.5D$ , the growth of structures in the wake appears to be primarily driven by turbine-induced structures, while for  $\mathcal{L}_x \gtrsim 1D$ ,

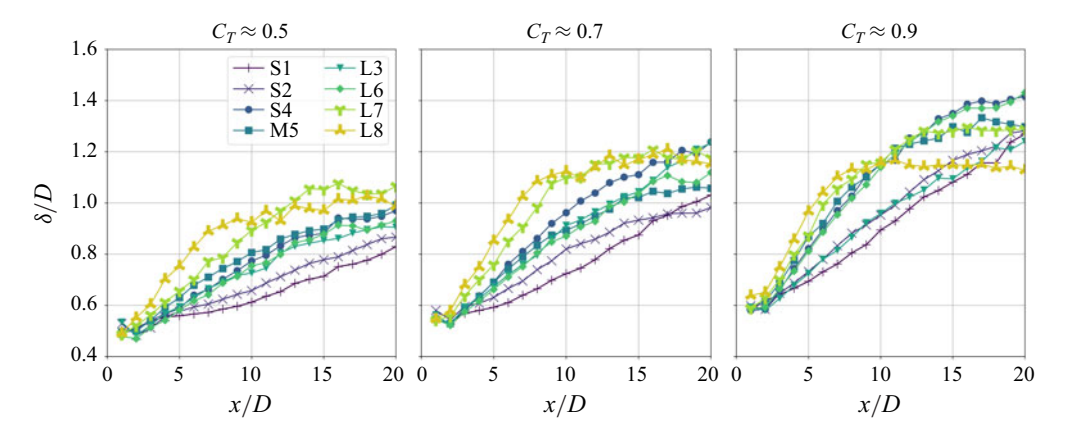


Figure 7. Streamwise evolution of the time-averaged wake width  $\delta(x)$ .

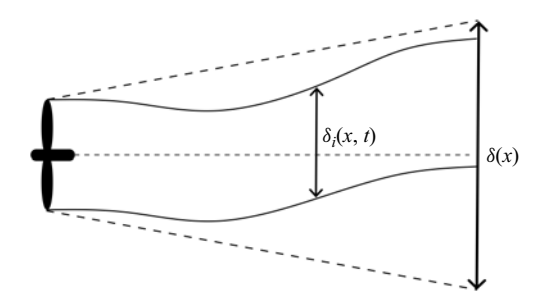


Figure 8. Sketch illustrating the contribution of wake meandering to the time-averaged wake width  $\delta(x)$ . Here,  $\delta_i(x,t)$  is the instantaneous wake width, determined from a single snapshot of the wake. Reproduced, with permission, from Kankanwadi & Buxton (2023).

the growth of wake structures is predominantly fuelled by the background flow. It should be noted, however, that this threshold may also depend on the spanwise ILS,  $\mathcal{L}_y$ , as well as on  $\Lambda$ , or  $C_T$ , whose effects cannot be separated in the present study.

## 3.2. Wake width and wake growth rate

## 3.2.1. Wake width based on the time-averaged velocity deficit $\Delta U$

Figure 7 shows the streamwise evolution of the time-averaged wake width,  $\delta(x)$ , for all 24  $\{C_T, \text{FST}\}$  combinations. At a given streamwise location x, the time-averaged wake width is defined as the radial location at which the time-averaged velocity deficit is 10 % that of the maximum, i.e.  $\delta(x)$  such that  $\Delta U(x, \delta) = 0.1 \Delta U_{max}(x)$ . Alternative thresholds and definitions of the wake width were tested and found not to change the evolution of  $\delta(x)$ . As illustrated in figure 8, two mechanisms contribute to the growth of the time-averaged wake width  $\delta(x)$ : (i) the physical growth of the instantaneous wake through the entrainment of background flow into the wake  $(\delta_i(x, t))$  increasing with x), and (ii) an apparent widening, in a time-averaged sense, resulting from the large-scale lateral displacement of the entire wake due to meandering. While we analyse this metric – widely used in engineering wind turbine wake models – without distinguishing the two contributions in that section, we will further discuss the influence of wake meandering on  $\delta(x)$  in § 3.5.

The most striking observation from figure 7 is the presence of a turning point in the slope of  $\delta(x)$  – particularly in highly turbulent inflows – beyond which the wake grows noticeably more slowly than upstream. All wakes initially grow linearly with streamwise distance, consistent with the frequently reported behaviour of wind turbine near wakes.

Most engineering wake models similarly assume a linear wake growth,  $\delta = \lambda x + \beta$ , with a wake growth rate  $\lambda$  that is independent of the streamwise position (e.g. Bastankhah & Porté-Agel 2014). However, our results show that this linear growth persists only up to a streamwise distance from the turbine that depends on  $C_T$  and the background turbulence. Except for the fully open grid case (S1), where wakes grow nearly linearly over the entire measurement range, a change in the slope of  $\delta(x)$  is observed for all FST cases, becoming sharper and occurring closer to the turbine as  $TI_{\infty}$  increases. Notably, in the highest- $TI_{\infty}$ case (L8), the wake width exhibits a quasi-asymptotic evolution for  $x/D \gtrsim 7$ , with  $\delta(x)$ approaching a plateau, whereas in the medium- $TI_{\infty}$  cases (group 2), the deceleration of the wake expansion is more progressive along the wake and begins farther downstream. Although observed for all  $C_T$ , this change in the wake expansion rate is more pronounced at higher  $C_T$ . Interestingly, the inflection point in  $\delta(x)$  for L8 approximately coincides with the downstream location where both TI and the turbine-added TKE have nearly homogenised with that of the background flow. The absence of a significant TKE and TI gradient between the wake and the ambient flow may lead to less efficient mixing and turbulent diffusion, ultimately resulting in reduced wake expansion rates.

Focusing on the near field  $(x/D \lesssim 7)$ , we observe a clear increase in  $\delta$  as both  $C_T$ and  $TI_{\infty}$  increase. Specifically, case L8 yields the widest wake, S1 the narrowest and the evolution of  $\delta$  follows the order  $\delta_{Group3} \geqslant \delta_{Group2} \geqslant \delta_{Group1}$ . Similarly, we observe that  $\delta_{High-C_T} \geqslant \delta_{Med-C_T} \geqslant \delta_{Low-C_T}$ , a trend that holds true for all measurement stations and FST cases. Focusing on the group 2 FST cases, we observe that  $\delta_{S4,M5} \geqslant \delta_{L3,L6}$ across the entire measurement range for  $C_T = 0.5$ , and up to  $x/D \approx 10$  for  $C_T \in \{0.7, 0.9\}$ . Since  $TI_{\infty,L6} \geqslant TI_{\infty,M5} \geqslant TI_{\infty,S4}$ , one might a priori expect that  $\delta_{S4,M5} \leqslant \delta_{L6}$ . However, given the considerably larger inflow ILS in cases L3 and L6 ( $\mathcal{L}_x \sim 2D$ ) compared with S4  $(\mathcal{L}_x \sim 0.5D)$  and M5  $(\mathcal{L}_x \sim 1D)$ , we may conclude that increasing the inflow ILS leads to a reduction in the time-averaged wake width in the near field. Interestingly, Kankanwadi & Buxton (2023) reported a reduction in the instantaneous near-wake width  $(\delta_i)$  downstream of a cylinder for inflows with large ILS, as well as a reduction in the timeaveraged wake width  $(\delta)$  for  $x/D \lesssim 3$ , in agreement with our results. Farther downstream  $(x/D \gtrsim 4)$ , however, they observed that wake meandering – enhanced by larger inflow ILS – compensated for the reduction in  $\overline{\delta_i}$ , yielding a larger  $\delta$  than in a non-turbulent inflow. In our experiments, wake meandering may not fully compensate for the decrease in  $\delta_i$ caused by larger inflow ILS – particularly at low  $C_T$ , where the higher rotor porosity may lead to weaker wake meandering – which could explain the observed reduction in  $\delta$  with increasing ILS within the group 2 cases. A more detailed analysis of large-scale wake motions will be presented in § 3.5.

In the far field, for group 3 FST cases, a quasi-plateau evolution of  $\delta$  is observed for all  $C_T$ . For group 2, a slowdown in the wake width growth is evident, whereas for group 1, the evolution remains nearly linear across the entire measurement range. Interestingly, for  $C_T = 0.9$ , the far-field wake width is larger in the lowest- $TI_{\infty}$  case (S1) than in the highest- $TI_{\infty}$  case (L8), which contrasts with the commonly reported trend that increasing  $TI_{\infty}$  leads to wider wind turbine wakes (though most studies have focused on the near field). This observation, however, aligns with recent findings on porous-disc wakes, where larger far wakes were observed for low-to-zero turbulence intensity inflows compared with high- $TI_{\infty}$  ones (Vinnes *et al.* 2023; Bourhis & Buxton 2024).

Figures 9(a) and 9(b) present the 24 wake growth rates  $\lambda = \langle d\delta/dx \rangle$ , calculated for two distinct intervals: one in the near field, calculated from the mean gradient of  $\delta(x)$  for  $2 \le x/D \le 7$ , and one in the far field, calculated from the mean gradient of  $\delta(x)$  for  $15 \le x/D \le 20$ . In the near field, we observe that  $\lambda$  increases with both  $C_T$  and  $TI_{\infty}$ . In this wake region, the variations in  $\lambda$  with  $C_T$  are more pronounced at high  $TI_{\infty}$  than at

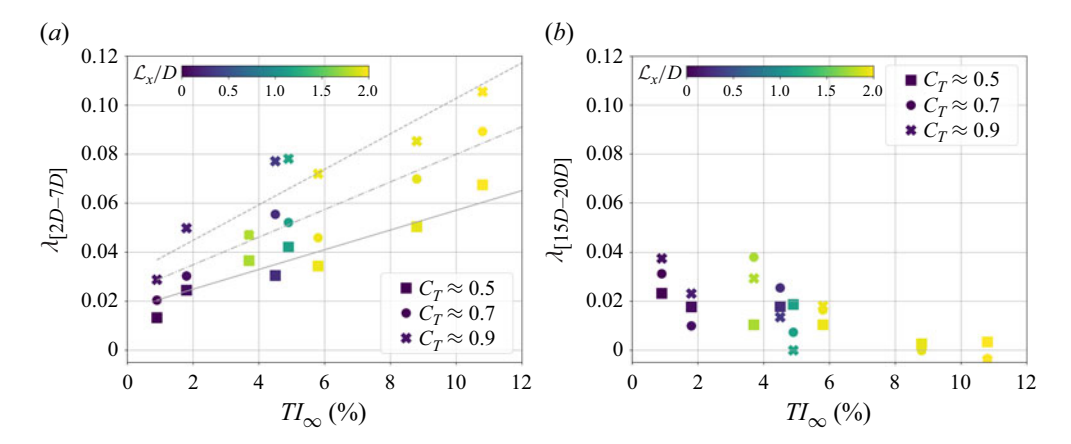


Figure 9. Wake growth rates calculated from  $\lambda = \langle d\delta/dx \rangle$  for (a)  $2 \le x/D \le 7$ , and (b)  $15 \le x/D \le 20$ .

low  $TI_{\infty}$ , with also larger differences between FST cases at higher  $C_T$ . While  $\mathcal{L}_x$  clearly affects the wake width  $\delta$ , its effect on  $\lambda$  appears secondary compared with  $TI_{\infty}$  and  $C_T$ . However, in the far wake  $x/D \ge 15$ , we observe the opposite trend: a decrease in  $\lambda$  as  $TI_{\infty}$ increases. Importantly, this change in how FST affects wind turbine wake spreading rates aligns with established entrainment behaviours for bluff and porous bodies. Kankanwadi & Buxton (2020, 2023) reported that both FST intensity and ILS enhance the entrainment and wake growth rates in cylinder near wakes, while FST intensity suppresses entrainment in the far wake. Moreover, Chen & Buxton (2023, 2024) identified a 'cross-over location' in cylinder wakes, located approximately 15D downstream (for the specific Reynolds number and FST 'flavour' parameter space studied), beyond which the wakes spread at a slower rate. Similarly, Vinnes et al. (2023), Bourhis & Buxton (2024) reported wider porous-disc wakes in the near field when exposed to FST, however, both wake growth and entrainment rates in the far field were found to decrease as FST intensity increased. The similar variation in wind turbine wake growth rates exposed to FST, along with the presence of a similar turning point in the wake width streamwise evolution further highlights the similarities between the entrainment behaviours observed in wind turbine and bluff-body wakes.

## 3.2.2. Modelling of the near-field wake growth rate $\lambda_{[2D-7D]}$

Meaningful insights can be drawn by comparing the near-field wake growth rate dataset,  $\lambda_{[2D-7D]}$  (figure 9a), with standard wake growth rate models. Early studies based on the top-hat Jensen velocity model assumed a constant growth rate: Jensen (1983) originally proposed  $\lambda = 0.1$ , while later work recommended  $\lambda = 0.075$  for onshore and  $\lambda = 0.03 - 0.05$  for offshore wind turbines (Mortensen *et al.* 2007; Barthelmie & Jensen 2010). Although these values broadly agree with our measurements, the assumption of a constant growth rate is clearly inadequate. In recent decades, more sophisticated wake growth rate models have emerged, typically obtained by fitting linear or power laws to  $\lambda$  datasets from LES, laboratory-scale experiments, or full-scale measurements. Several studies report a linear relationship between the wake growth rate and  $TI_{\infty}$ , as  $\lambda = aTI_{\infty} + b$ , with varying  $\{a, b\}$  coefficients: Niayifar & Porté-Agel (2016) found a = 0.38 and b = 0.004 (LES); Carbajo Fuertes, Markfort & Porté-Agel (2018) obtained a = 0.35 and b = 0 (field measurements); and Cheng *et al.* (2019) reported a = 0.223 and b = 0.022 (LES). These empirical relationships were obtained with turbines operating at

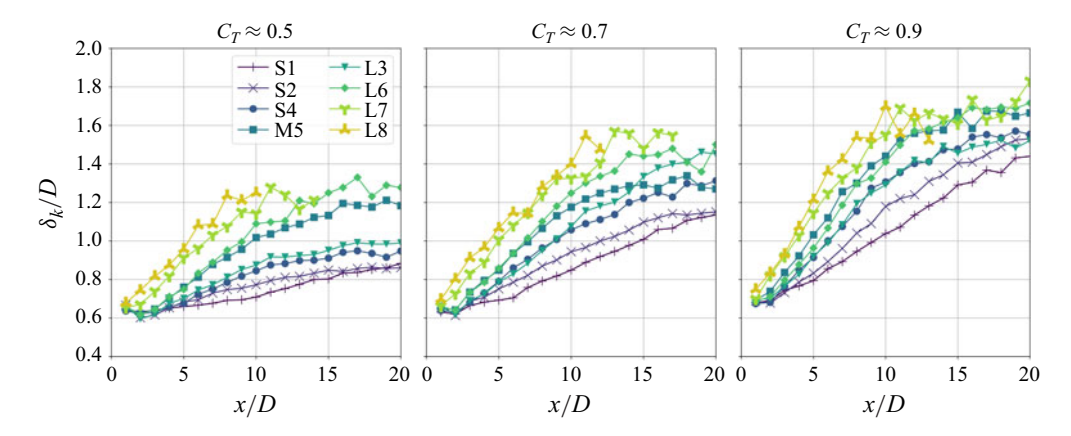


Figure 10. Streamwise evolution of the wake width based on the turbine-added TKE,  $\delta_k$ .

a single  $C_T$  ( $C_T \approx 0.8$ ) and do not consider the influence of the FST length scale. Fitting  $\lambda = aTI_{\infty} + b$  to the entire  $\lambda_{[2D-7D]}$  dataset yields a poor fit ( $R^2 = 0.621$ , with a = 0.592 and b = 0.022), mainly due to the strong dependence of  $\lambda_{[2D-7D]}$  on  $C_T$ . When  $C_T$  cases are treated separately, the fits improve substantially, supporting a linear relationship between  $TI_{\infty}$  and  $\lambda_{[2D-7D]}$ . For example, for  $C_T \approx 0.5$ , a = 0.47, b = 0.013 ( $R^2 = 0.907$ ); for  $C_T \approx 0.7$ , a = 0.62, b = 0.019 ( $R^2 = 0.929$ ); and for  $C_T \approx 0.9$ , a = 0.68, b = 0.033 ( $R^2 = 0.850$ ). Building on these observations, we fitted the combined model to the full dataset:  $\lambda_{[2D-7D]} = aC_TTI_{\infty} + bC_T + c\mathcal{L}_x$ , obtaining a = 0.83, b = 0.032,  $c \sim 10^{-11}$ , and a significantly improved  $R^2 = 0.914$  (grey lines in figure 9a). This empirical model provides a reasonable approximation of the wake growth rate in the near field, while further highlighting the negligible influence of  $\mathcal{L}_x$  compared with  $TI_{\infty}$  and  $C_T$ .

Recently, Ishihara & Qian (2018) proposed the following empirical power-law wake growth rate model based on LES data,  $\lambda = 0.11 C_T^{1.07} T I_\infty^{0.2}$ , which yields a poor fit with the current dataset ( $R^2 = 0.343$ ). Taking inspiration from this model, we fitted a similar power law:  $\lambda_{[2D-7D]} = a C_T^{\alpha_1} T I_\infty^{\alpha_2} \mathcal{L}^{\alpha_3}$ , resulting in  $\lambda_{[2D-7D]} = 0.372 C_T^{0.99} T I_\infty^{0.53}$  ( $\alpha_3 \sim 10^{-11}$ ) with  $R^2 = 0.923$ . While the  $C_T$  exponent closely matches that of Ishihara & Qian (2018), our model shows a stronger dependence on  $TI_\infty$ . Our dataset includes eight FST intensity levels, compared with two in their study, which may explain the reduced sensitivity observed in their model.

Finally, both the linear and power-law fit models provide fairly good approximations of  $\lambda_{[2D-7D]}$  across a wide range of  $C_T$  and FST condition. While small  $R^2$  differences prevent favouring one over the other, they clearly outperform most existing models, which are usually calibrated for a single  $C_T$  and based on much smaller datasets.

#### 3.2.3. Wake width based on the turbine-added TKE $\Delta k$

Analogous to the velocity deficit-based wake width  $\delta$ , we define a characteristic wake width  $\delta_k$  based on the turbine-added TKE  $\Delta k$ . At a given streamwise location x,  $\delta_k$  is defined as the radial location where  $\Delta k(x,\delta_k)=0.1\Delta k_{max}(x)$ . For the two highest  $TI_{\infty}$  cases (L7 and L8), the  $\Delta k$  profiles become nearly flat in the far field; therefore, to ensure meaningful wake identification, we define a TKE-based wake only when  $\Delta k_{max}/U_{\infty}^2>0.001$ . The expansion rates of the TKE-based wakes,  $\lambda_k=\langle \mathrm{d}\delta_k/\mathrm{d}x\rangle$ , are computed in the near and far fields from the mean gradient of  $\delta_k$  for  $2\leqslant x/D\leqslant 7$  ( $\lambda_{k[2D-7D]}$ ), and  $15\leqslant x/D\leqslant 20$  ( $\lambda_{k[15D-20D]}$ ), respectively. Figures 10 and 11 show the streamwise evolution of  $\delta_k(x)$  and the TKE-based expansion rates,  $\lambda_k$ , for all 24 { $C_T$ , FST} combinations.

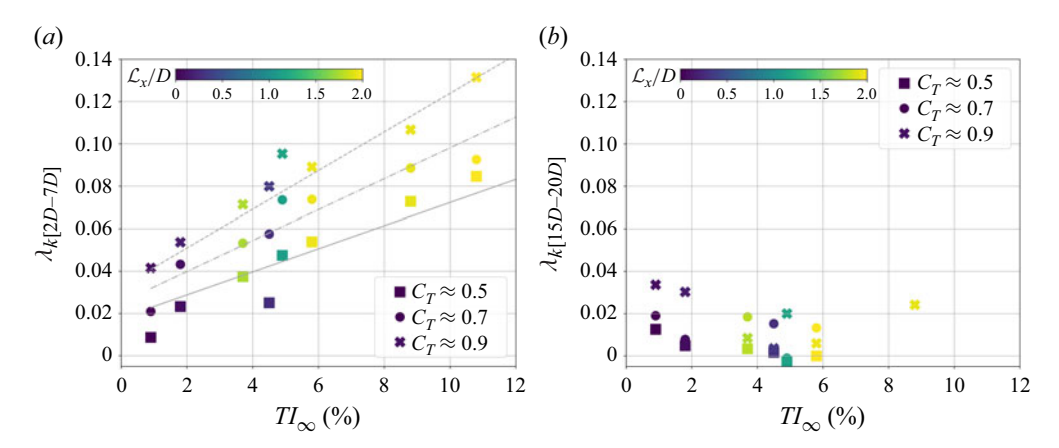


Figure 11. Wake growth rates calculated from  $\lambda_k = \langle d\delta_k/dx \rangle$  for (a)  $2 \le x/D \le 7$ , and (b)  $15 \le x/D \le 20$ .

First, the behaviour of  $\delta_k(x)$  closely mirrors that of  $\delta(x)$ . The TKE-based wakes grow nearly linearly in the near field before reaching a plateau, with larger  $TI_{\infty}$  leading to steeper slopes and sharper transitions to the plateau region. Like  $\delta$ ,  $\delta_k$  increases as both  $C_T$  and  $TI_{\infty}$  increase, with  $\delta_{k,High-C_T} \geqslant \delta_{k,Med-C_T} \geqslant \delta_{k,Low-C_T}$  and  $\delta_{k,Group3} \geqslant \delta_{k,Group2} \geqslant \delta_{k,Group1}$ , while  $\mathcal{L}_x$  has only a secondary influence. Moreover, the  $\lambda_{k[2D-7D]}$  distribution shown in figure 11(a) closely aligns with that of  $\lambda_{[2D-7D]}$  in figure 9(a), though with larger values. Hence, fitting the  $\lambda_{k[2D-7D]}$  dataset with the same model used for  $\lambda_{[2D-7D]}$  yields a good fit ( $R^2 = 0.931$ ):  $\lambda_{k[2D-7D]} = 0.92C_TTI_{\infty} + 0.037C_T + 0.004\mathcal{L}$  (grey lines in figure 11a).

The TKE-based wakes are wider than the velocity deficit-based wakes,  $\delta_k(x) \ge \delta(x)$ , and expand faster,  $\lambda_{k[2D-7D]} \geqslant \lambda_{[2D-7D]}$ , with more pronounced differences at high  $TI_{\infty}$ and large  $C_T$ . This further emphasises the faster turbulent mixing of the TKE in the wake with the background TKE compared with mass and momentum in the near field, consistent with previous studies on porous and bluff-body wakes (Buxton & Chen 2023; Lingkan & Buxton 2023). The reduced growth of  $\delta_k$  mirrors that of  $\delta$ , and occurs when the difference in TKE between the wake and the ambient flow becomes shallower, highlighting the important role of  $\Delta k$  in driving wake expansion and recovery. Once  $\Delta k$  becomes small, both the TKE and velocity deficit expansion rates are reduced, explaining the smaller  $\lambda_k$ and  $\lambda$  in the far field, especially for high- $TI_{\infty}$  inflows (figure 11b). Hence, FST intensity accelerates the dissipation of the turbine-added TKE and the recovery of the velocity in the near field. However, the TKE recovers more quickly, eventually reaching a quasiuniform state for high- $TI_{\infty}$  inflows. Once  $\Delta k \approx 0$ , the recovery of the velocity deficit slows significantly as it propagates through a region of nearly homogeneous TKE, reducing momentum and mass transfer from the background flow into the wake and limiting further wake recovery.

#### 3.3. Evolution of wake-averaged quantities

#### 3.3.1. Wake velocity recovery

The influence of FST on the wake velocity recovery is assessed following the approach of Li, Dong & Yang (2022) and Messmer *et al.* (2024) by radially averaging the time-averaged velocity from the wake centre to the wake width  $\delta(x)$ , i.e.  $\widetilde{U}(x) = \langle \overline{U}(x, y) \rangle_{\delta(x)}$ . Here,  $\widetilde{U}(x)$  is the mean time-averaged velocity within a streamtube of width  $\delta(x)$ , with

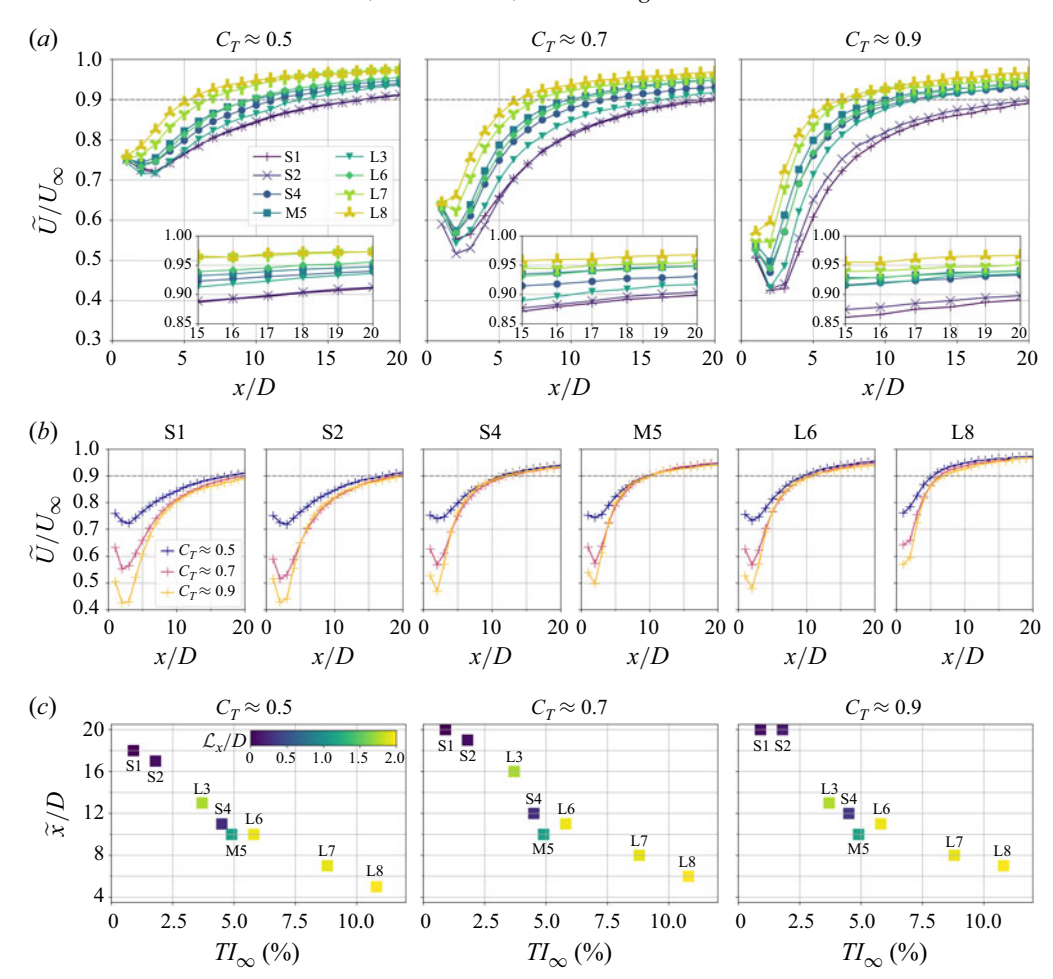


Figure 12. Streamwise evolution of the wake velocity recovery,  $\widetilde{U}/U_{\infty}$ , with a focus on the influence of FST in panel (a), and of  $C_T$  in panel (b). Panel (c) shows the streamwise distance,  $\widetilde{x}$ , required for the wake to recover to  $\widetilde{U}(\widetilde{x}) = 0.9U_{\infty}$ .

 $\widetilde{U}/U_{\infty}$  approaching unity as the wake recovers. Since the power available to a downstream turbine virtually operating in the wake of another scales as  $\widetilde{P}_a/P_{\infty} \propto (\widetilde{U}/U_{\infty})^3$ ,  $\widetilde{U}(x)$  also serves as a measure of wake-induced power loss. In addition, we define  $\widetilde{x}$  as the streamwise distance at which the wake recovers to  $\widetilde{U}(\widetilde{x}) = 0.9U_{\infty}$  (i.e.  $\widetilde{P}_a(\widetilde{x}) = 0.72P_{\infty}$ ), providing a quantitative – albeit somewhat arbitrary – measure of the near-wake streamwise extent, which we use to compare the different cases.

Figure 12 shows  $\widetilde{U}(x)$  and  $\widetilde{x}$  for all 24 { $C_T$ , FST} combinations. For both group 1 and 2 cases,  $\widetilde{U}/U_{\infty}$  initially decreases for  $x/D \leqslant 2$ , reflecting the pressure recovery in the very near wake. As with porous discs, higher  $C_T$  increases flow blockage, resulting in a larger pressure drop and a stronger reduction in  $\widetilde{U}/U_{\infty}$  immediately downstream of the turbine. For all cases,  $\widetilde{U}/U_{\infty}$  increases rapidly in the near field ( $3 \lesssim x/D \lesssim 7$ ) before transitioning to a slower recovery rate further downstream. The largest differences in  $\widetilde{U}/U_{\infty}$  between FST cases are observed in the near field and become more pronounced with increasing  $C_T$ . The wake-averaged velocity recovery is significantly enhanced as  $TI_{\infty}$  increases, with a clear distinction between  $TI_{\infty}$  groups:  $(\widetilde{U}/U_{\infty})_{Group3} \geqslant (\widetilde{U}/U_{\infty})_{Group2} \geqslant (\widetilde{U}/U_{\infty})_{Group1}$ 

(for all  $C_T$  and x/D), and  $\widetilde{x}_{Group3} \leqslant \widetilde{x}_{Group2} \leqslant \widetilde{x}_{Group1}$ . Wakes exposed to high- $TI_{\infty}$  inflows exhibit rapid near-field recovery, as evidenced by the steep  $\widetilde{U}$  gradient over the first few diameters, whereas wakes developing in low- $TI_{\infty}$  inflows recover more gradually. Closer examination of group 2 cases reveals that  $\widetilde{U}/U_{\infty}$  deviates from the strict  $TI_{\infty}$  hierarchy, indicating that FST ILS also plays a role in the velocity recovery. For all  $C_T$ ,  $(\widetilde{U}/U_{\infty})_{M5} \geqslant (\widetilde{U}/U_{\infty})_{L6}$  within specific streamwise ranges: up to  $x/D \approx 10$  at  $C_T \approx 0.5$ , and up to  $x/D \approx 15$  at  $C_T \in \{0.7, 0.9\}$ , consistent with the earlier observation of  $(\Delta U/U_{\infty})_{max,M5} \leqslant (\Delta U/U_{\infty})_{max,L6}$ . Additionally, for  $C_T \approx 0.9$ ,  $(\widetilde{U}/U_{\infty})_{L6} \approx (\widetilde{U}/U_{\infty})_{S4}$  in the near field. Given that  $TI_{\infty,L6} \geqslant TI_{\infty,M5} \geqslant TI_{\infty,S4}$  and  $\mathcal{L}_{x,L6} \geqslant \mathcal{L}_{x,M5} \geqslant \mathcal{L}_{x,S4}$ , these observations highlight the role of the FST ILS in slowing the recovery of the wake-averaged velocity. Finally, in the near field,  $\widetilde{U}/U_{\infty}$  is markedly lower for case L3 than for case S4, despite comparable FST intensities. Whilst the slightly lower  $TI_{\infty}$  in case L3 may partly account for the delayed velocity recovery, the pronounced difference in  $\widetilde{U}/U_{\infty}$  between the two cases is likely also a consequence of the larger inflow ILS in L3.

Figure 12(b) highlights the influence of  $C_T$  on  $\widetilde{U}/U_\infty$  across 6 different FST cases. In the near field  $(x/D \lesssim 10)$ , the recovery rate of  $\widetilde{U}/U_\infty$  increases substantially with  $C_T$ . Further downstream, the  $\widetilde{U}/U_\infty$  curves nearly collapse, especially in the presence of FST. Larger and prolonged differences in  $\widetilde{U}/U_\infty$  between the  $C_T$  cases are observed in low- $II_\infty$  inflow conditions (S1 & S2), whereas higher  $II_\infty$  rapidly mitigates the additional velocity deficit induced by higher  $II_\infty$  Hence, varying  $II_\infty$  rapidly modifies the nearfield wake-averaged velocity and recovery rate, with a diminishing influence as  $II_\infty$  increases. Figure 12(c) shows that  $II_\infty$  decreases dramatically with increasing FST intensity, exhibiting significantly greater sensitivity to  $II_\infty$  than to  $II_\infty$  and  $II_\infty$  although  $II_\infty$  increases slightly with  $II_\infty$ . For the lowest  $II_\infty$  case, S1, at  $II_\infty$  and  $II_\infty$  he wake-averaged available power has not yet reached 72% of the free stream available power  $II_\infty$ , even at 20D, whereas for L8,  $II_\infty$  for all  $II_\infty$ . Generally, in weakly turbulent background flows,  $II_\infty$  variations generate persistent effects on the wake velocity recovery that extend into the far field, whilst in highly turbulent conditions, these effects are rapidly attenuated with FST intensity promoting near-field velocity recovery.

#### 3.3.2. Turbine-added TKE dissipation

Similarly to  $\widetilde{U}$ , we define the wake-averaged TKE,  $\widetilde{k}(x) = \langle \overline{k}(x,y) \rangle_{\delta(x)}$ . Since the background TKE,  $k_{\infty}$ , varies across the FST cases, the recovery of the TKE within the wakes is assessed using the wake-averaged turbine-added TKE,  $\Delta \widetilde{k}/U_{\infty}^2 = (\widetilde{k} - k_{\infty})/U_{\infty}^2$ , with  $\Delta \widetilde{k}$  approaching 0 indicating a higher degree of wake TKE recovery. We also introduce  $\widetilde{x}_k$ , the TKE-based near-field length, defined as the streamwise distance at which  $\Delta \widetilde{k}(\widetilde{x}_k)/U_{\infty}^2 = 0.0015$ . Figure 13 presents  $\Delta \widetilde{k}(x)/U_{\infty}^2$  and  $\widetilde{k}(x)/U_{\infty}^2$ , along with  $\widetilde{x}_k$  for all 24 { $C_T$ , FST} combinations.

Both k and  $\Delta k$  immediately downstream of the rotor increase with  $C_T$ . For  $C_T = 0.5$ , both quantities decay for  $x/D \ge 1$ , whereas at  $C_T \in \{0.7, 0.9\}$ , k and k first increase with streamwise distance, likely due to the stronger tip shear layer, which enhances turbulence production behind the rotor (see figure 5). As  $C_T$  and  $TI_\infty$  increase, the streamwise location where k and k begin to decay shifts closer to the turbine, aligning with porousdisc wakes (Li *et al.* 2024). As shown in figure 13(a), the decay of k in case L3 (k) begins further downstream compared with cases with similar k but smaller k - S4 (k) and M5 (k) - suggesting that the TKE recovery onset is delayed when increasing the inflow ILS, though the lowest k for L3 may partly explain this delay. Larger differences in k between the k cases persist in the far field in low-k inflow conditions (e.g. see cases S1

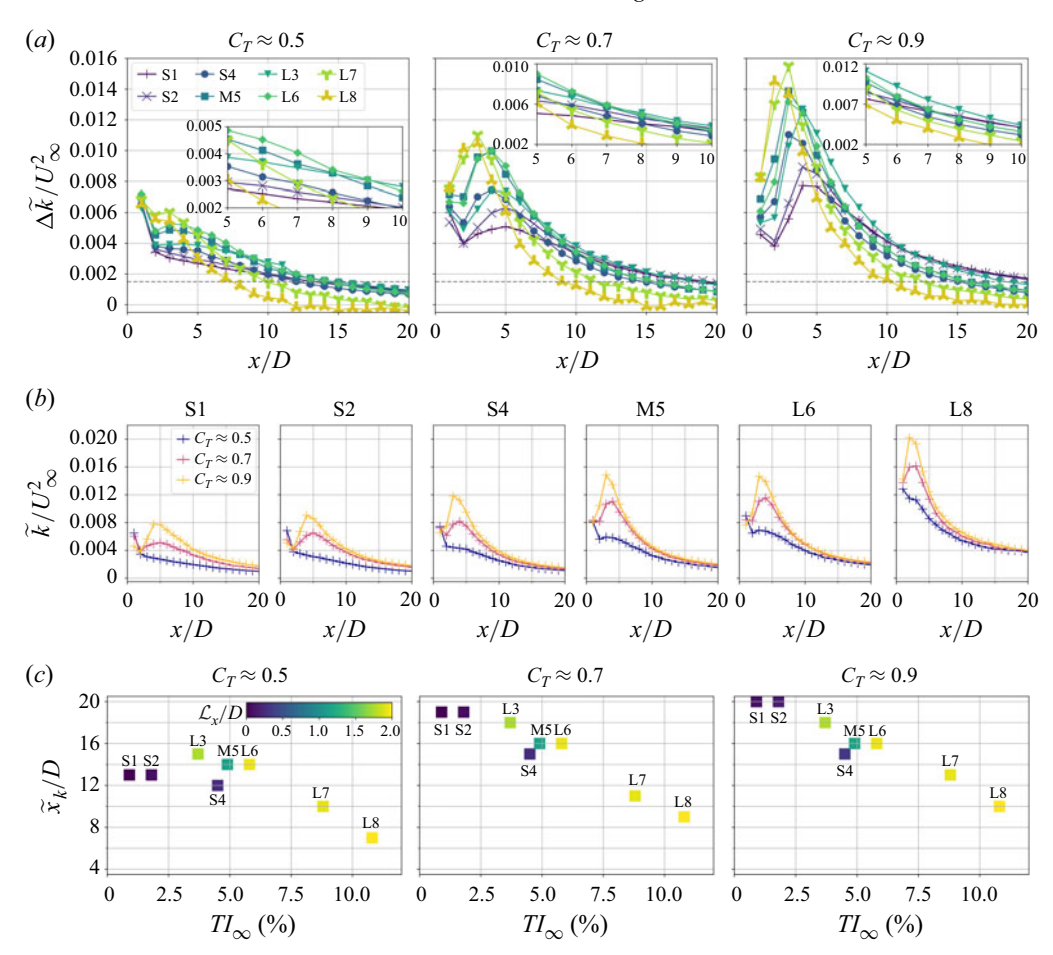


Figure 13. Streamwise evolution of the wake-averaged turbine-added TKE,  $\Delta \widetilde{k}/U_{\infty}^2$  (a), and wake-averaged TKE,  $\widetilde{k}/U_{\infty}^2$  (b). A focus is placed on the influence of FST in panel (a), and of  $C_T$  in panel (b). Panel (c) shows the streamwise distance,  $\widetilde{x}_k$ , required for the wake to recover to  $\Delta \widetilde{k}(\widetilde{x}_k)/U_{\infty}^2 = 0.0015$ .

and S2 in figure 13b), highlighting the prolonged sensitivity of the TKE recovery to  $C_T$  variations in weakly turbulent ambient flows.

For all  $C_T$ , the maximum  $\Delta k$  follows the order:  $(\Delta k/U_\infty^2)_{max,Group3} \geqslant (\Delta k/U_\infty^2)_{max,Group2} \geqslant (\Delta k/U_\infty^2)_{max,Group1}$ , although it does not strictly follow the hierarchical order of increasing  $TI_\infty$ , due to the secondary influence of  $C_T$  and  $\mathcal{L}_x$ . The recovery rate of  $\Delta k$  is largely a function of  $TI_\infty$ , with the fastest recovery in case L8 and the slowest in case S1. As previously observed in the TKE profiles,  $\Delta k \approx 0$  for case L8 at  $x/D \gtrsim 15$  across all three  $C_T$  cases. Focusing on L# cases,  $\Delta k/U_\infty^2$  follows a hierarchical order corresponding to decreasing  $TI_\infty$  after a few diameters, i.e.  $(\Delta k/U_\infty^2)_{L8} \leqslant (\Delta k/U_\infty^2)_{L7} \leqslant (\Delta k/U_\infty^2)_{L6} \leqslant (\Delta k/U_\infty^2)_{L3}$  (for all  $C_T$ ), with a similar trend observed for S# cases. This clearly illustrates that the recovery of the turbine-added TKE is enhanced with increasing  $TI_\infty$ . The local recovery rate also varies as the wake mixes with the background flow and  $\Delta k$  decays. The TKE recovery is accelerated in the near field for high- $TI_\infty$  and high- $C_T$  cases, driven by enhanced mixing resulting from both higher FST intensity and a greater initial  $\Delta k$ , whilst the recovery is more gradual for low- $TI_\infty$  and low- $C_T$  cases.

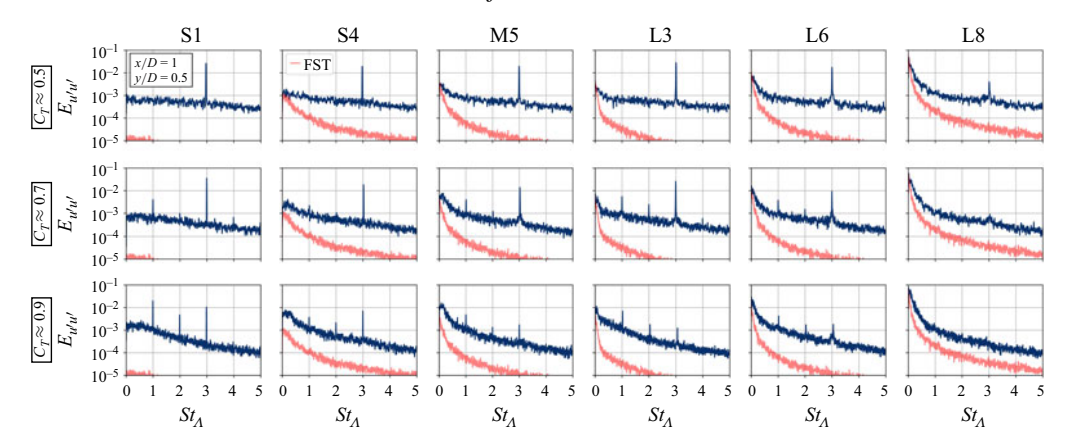


Figure 14. Power spectra of the velocity fluctuations  $E_{u'u'}$  as a function of the Strouhal number  $St_{\Lambda} = f/f_{r}$ . Spectra are computed in the tip shear layer and at the first measurement station,  $\{x/D, y/D\} = \{1, 0.5\}$ . The FST power spectra, measured without the turbine at  $\{x/D, y/D\} = \{0, 0\}$ , are shown in red.

Focusing on group 2 FST cases – L6 (•), M5 (•) and S4 (•) – it is observed that for all  $C_T$ ,  $(\Delta \widetilde{k}/U_\infty^2)_{L6} \geqslant (\Delta \widetilde{k}/U_\infty^2)_{M5} \geqslant (\Delta \widetilde{k}/U_\infty^2)_{S4}$  for  $x/D \gtrsim 5$  (figure 13a). This trend may seem counter-intuitive, as one might expect the opposite given the earlier conclusion that higher  $TI_\infty$  promotes the faster decay of the turbine-added TKE. However, given that  $\mathcal{L}_{x,L6} \approx 2\mathcal{L}_{x,M5} \approx 4\mathcal{L}_{x,S4}$ , this suggests that larger ILS slows the TKE recovery for inflows with nearly identical  $TI_\infty$ . Moreover, the substantially larger  $\Delta \widetilde{k}/U_\infty^2$  for case L3 (•) compared with case S4 (•), despite both cases having nearly identical  $TI_\infty$ , further reinforces that the TKE recovery is delayed and slower as the inflow ILS increases.

Finally, the TKE-based near-field length  $\widetilde{x}_k$  increases with  $C_T$  due to greater initial turbine-added TKE, but decreases substantially with increasing  $TI_{\infty}$  (figure 13c). Comparison of group 2 cases reveals that  $\widetilde{x}_k$  increases with  $\mathcal{L}_x - \widetilde{x}_{k,L3} \geqslant \widetilde{x}_{k,L6,M5} \geqslant \widetilde{x}_{k,S4}$  – confirming the slower recovery of the turbine-added TKE when increasing the background ILS.

#### 3.4. Near-wake dynamics

Figure 14 shows the power spectra of the velocity fluctuations,  $E_{u'u'}$ , computed in the nearwake tip shear layer at  $\{x/D, y/D\} = \{1, 0.5\}$ . In this figure, the Strouhal number is defined as  $St_{\Lambda} = \pi St_{D}/\Lambda = f/f_{r}$ , where  $f_{r}$  is the rotor rotational frequency and  $St_{D} = fD/U_{\infty}$ .

For the lowest tip-speed ratio ( $C_T \approx 0.5$ ,  $\Lambda = 1.7$ ), the dominant frequency for all FST cases is  $St_A = 3$ , which corresponds to the blade passage frequency,  $3f_r$ . As  $C_T$  and  $\Lambda$  increase, additional peak frequencies – multiples of the rotor rotational frequency – appear, notably  $1f_r$  ( $St_A = 1$ ) and  $2f_r$  ( $St_A = 2$ ). In general, as  $\Lambda$  increases, the spectral amplitude of the  $3f_r$  peak decreases, while those of the  $1f_r$  and  $2f_r$  peaks become more pronounced and progressively dominate over  $3f_r$ . No clear influence of  $\mathcal{L}_x$  is observed, but higher  $TI_\infty$  significantly reduces the spectral amplitude at all three leading frequencies. For instance, for the highest  $TI_\infty$  case (L8), no distinct spectral peaks are observed at x/D = 1 for the two highest  $\Lambda$ . Spectrograms in figure 15(a) further highlight the rapid dissipation of high-frequency rotor-related structures with increasing  $TI_\infty$ .

The spectrograms shown in figure 15(b) illustrate the spanwise extent of the turbinerelated coherent motions at x/D = 1. Interestingly, for the lowest tip-speed ratio ( $C_T \approx$  0.5),  $3f_r$  is observed across almost the entire blade span ( $0 \le y/D \le 0.5$ ), with its spectral amplitude being more pronounced near the wake edge ( $y/D \approx 0.5$ ) and close to the wake centreline ( $y/D \approx 0.1$ ), highlighting the presence of tip and root vortices. The presence of

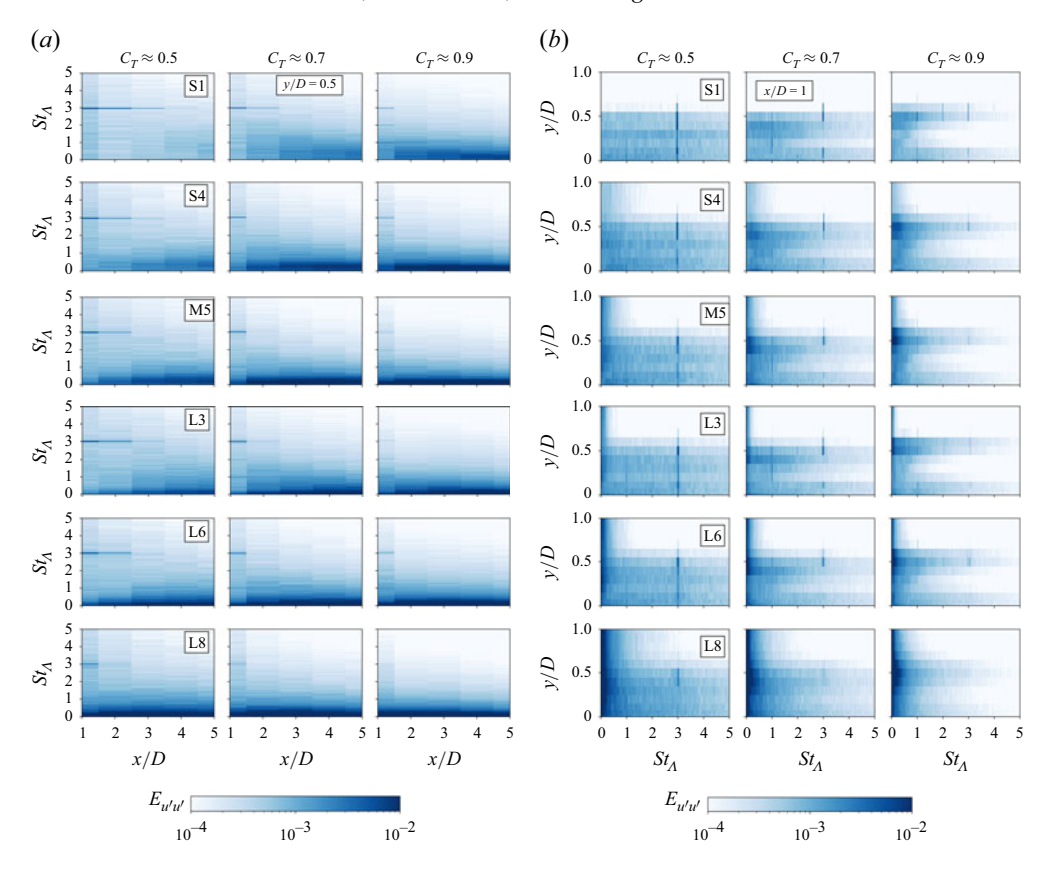


Figure 15. Spectrograms of the velocity fluctuations computed at y/D = 0.5 for  $1 \le x/D \le 5$  (a), and at x/D = 1 for  $0 \le y/D \le 1$  (b).

 $3f_r$  in the mid-span blade region emphasises the existence of the vortex sheet shed from the trailing edge of the rotor blades that connects tip and root vortices. It is noteworthy that, in the wind turbine vortex system proposed by Okulov & Sørensen (2007), the tip vortices are assumed to be embedded within a helical vortex field, formed by the blade's trailing edge vortex sheet and root vortices, which appears to align with the spectrograms obtained with the turbine operating at the lowest tip-speed ratio. For  $C_T \in \{0.7, 0.9\}$ , the presence of  $3f_r$  is confined to the tip shear layer and near the root of the blade, with no indication of the trailing edge vortex sheet, suggesting either its early dissipation or that it never formed. As previously mentioned, increasing  $\Lambda$  leads to the emergence of multiple rotor-related frequencies, with their spanwise existence varying depending on  $C_T$  and the FST. Notably, at  $C_T \approx 0.9$ ,  $1f_r$ ,  $2f_r$ ,  $3f_r$ , along with a small trace of  $4f_r$ , are observed in both the tip  $(y/D \approx 0.5)$  and root  $(y/D \approx 0.1)$  regions for the weakest turbulent background case (S1). The amplitudes of these frequencies decay with increasing  $TI_{\infty}$ , with faster dissipation near the root, indicating that root vortices are weaker and diffuse more rapidly than tip vortices, while FST enhances the dissipation of both. Specifically, no traces of  $\Lambda$ -dependent high-frequency structures are observed for case L8 at  $C_T \approx 0.9$  and x/D = 1, underscoring the significant and immediate influence of FST on these structures. For low and moderate  $TI_{\infty}$  cases (S1, S4, M5 and L3) at  $C_T \approx 0.7$ ,  $1f_T$  spans nearly the entire blade span, suggesting the presence of a vortex sheet analogous to the one observed at  $3f_r$  for  $C_T \approx 0.5$ , though of lower frequency and strength.

Except for the most turbulent case L8, the spectra in figure 14 are qualitatively similar across FST cases for a given  $C_T$ , with variations in the amplitude of the spectral peaks reflecting the influence of  $II_{\infty}$  on vortex strength and dissipation. Thus, the existence of specific turbine-related coherent modes in the near field is governed primarily by the tip-speed ratio and only weakly influenced by the incoming turbulence, although the FST accelerates their energy decay. The presence of multiple peaks at  $\{1f_r, 2f_r, 3f_r\}$ for  $C_T \in \{0.7, 0.9\}$  in the tip shear layer suggests that the breakdown of the tip-vortex structure follows a multi-step mechanism, in which consecutive helical vortex filaments interact and merge before losing coherence and dissipating (Felli, Camussi & Di Felice 2011; Sherry et al. 2013; Biswas & Buxton 2024b). For  $C_T \approx 0.5$  only the  $3f_r$  mode is observed, suggesting that tip vortices primarily dissipate and mix with the surrounding flow without interacting with one another. Biswas & Buxton (2024b) found that the triadic energy exchanges between harmonics of  $f_r$  – which drive the tip-vortex merging process – are significantly weakened at low tip-speed ratios, because of the larger spacing between consecutive filaments. Given that the turbine operates at a very low tip-speed ratio ( $\Lambda = 1.7$ ) for  $C_T \approx 0.5$  in our experiments, consecutive filaments may be too widely spaced to interact. Alternatively, the energy content of the coherent motion resulting from their merging may be too low to be discernible in the spectra.

#### 3.5. Statistics and dynamics of wake meandering

Wake meandering describes the large-scale, low-frequency motions of the wake, typically occurring in the far wake (Yang & Sotiropoulos 2019). When performing horizontal scans of wakes, it manifests through the large lateral motion of the wake centreline (note that the amplitude of vertical meandering is typically found to be smaller than lateral meandering (Hodgson, Madsen & Andersen 2023; Vahidi & Porté-Agel 2024)). This dynamic has been linked to the presence of a low-frequency broad peak in the velocity spectra, within the range  $St_D \in [0.1, 0.4]$ , which is influenced by  $\Lambda$ ,  $C_T$  and the FST conditions (Chamorro & Porté-Agel 2009; Biswas & Buxton 2024a). Two possible origins of wake meandering have been proposed in the literature: the passive advection of the wake by large-scale atmospheric eddies, or an intrinsic shear-layer instability analogous to vortex shedding from bluff or porous bodies.

Wake meandering is analysed through the wake centre position statistics and the power spectra in the low-frequency range ( $St_D \in [0, 1]$ ). At each x/D, the 240 s time series from the 21 hot-wires are divided into 2400 bins of 0.1 s each. In each  $21 \times 0.1$  s bin, the wake centre position  $y_c$  is taken as the radial location (among the 21 hot-wire positions) of minimal velocity. If the wake centre position is found at y < 0, the data are discarded due to the asymmetric sensor arrangement that provides better spatial resolution for  $y \ge 0$ . The 0.1 s bin width was chosen based on the diameter-based Strouhal number typically reported for wake meandering,  $St_D \approx 0.2$  ( $\approx 2$  Hz in our experiments), satisfying the Nyquist–Shannon criterion and ensuring that the analysis focuses on the influence of large-scale, low-frequency structures on the wake centre positions. The probability density functions of wake centre positions, p.d.f.( $y_c/D \ge 0$ ), are compared for different { $C_T$ , FST} combinations in figure 16(a). Figures 16(b) and 16(c) show the standard deviation of the wake centreline  $\sigma_{y_c}(x)/D$ , with the first figure emphasising the influence of  $C_T$ , and the second highlighting the effects of FST.

First, for all  $\{C_T, FST\}$  cases, the p.d.f. of the wake centre positions becomes progressively flatter, broader and develops more pronounced tails with increasing x/D. This indicates greater variability in the wake's lateral position, with more frequent significant deviations from the mean centreline. The central peak is strongest for case S1 and weakest for case L8, showing that wakes exposed to FST experience larger deviations

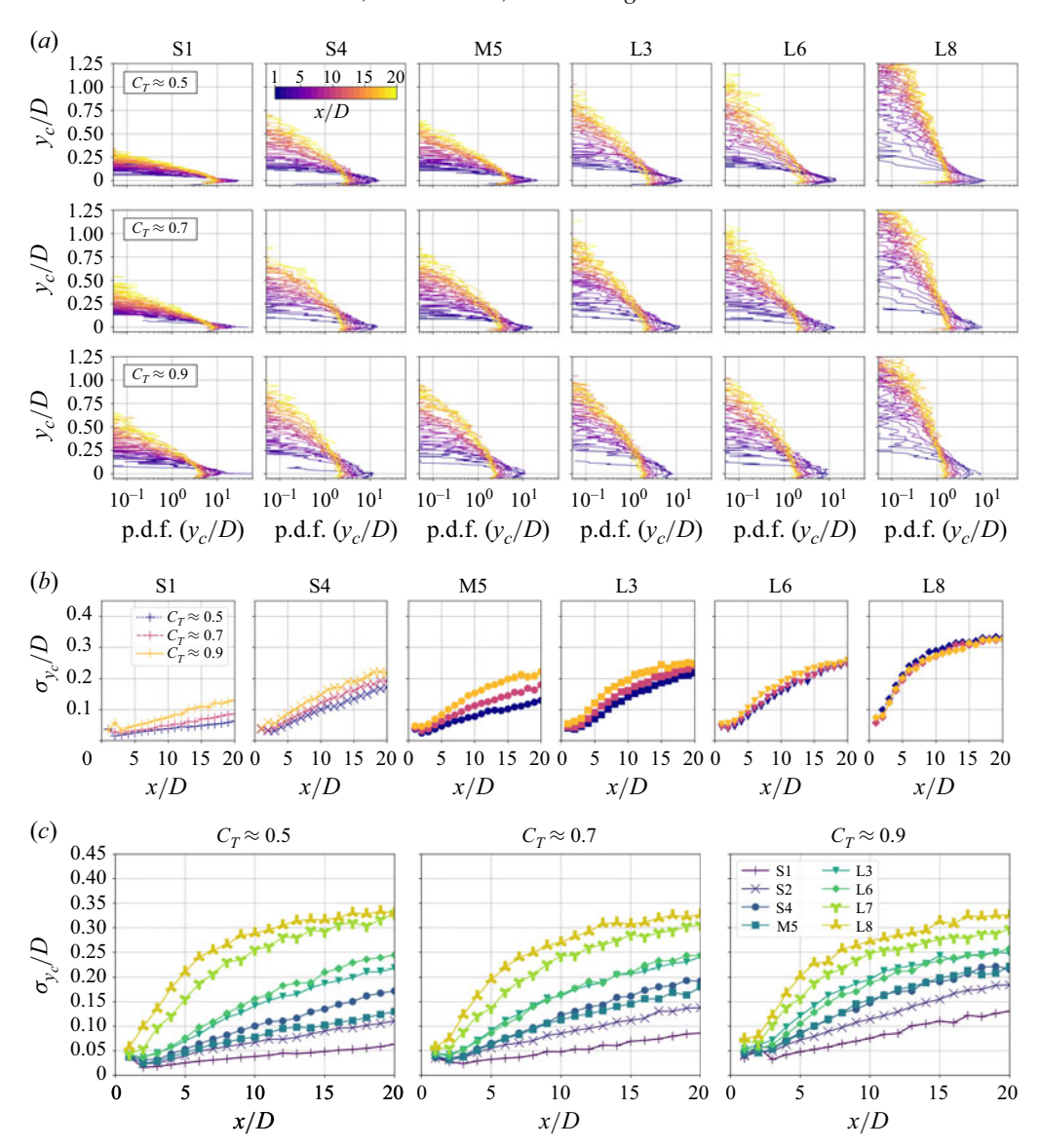


Figure 16. Probability density functions, p.d.f.  $(y_c/D)$  (a), and standard deviations,  $\sigma_{y_c}/D$  (b and c) of the wake centre positions. A focus is placed on the influence of  $C_T$  on  $\sigma_{y_c}/D$  in panel (b), and of FST in panel (c).

from their time-averaged trajectory. Additionally, the flatness of the p.d.f. increases with both  $TI_{\infty}$  and  $\mathcal{L}_x$ , deviating progressively from a Gaussian distribution with increasingly pronounced tails. This highlights the role of FST in amplifying wake meandering, with a higher likelihood of wake centreline deviations from the mean position, larger lateral displacements and increasingly irregular wake motions over time. We also observe a strong influence of  $C_T$  on the p.d.f.: as  $C_T$  increases, the central peak diminishes, the distribution broadens, and the tails become heavier. The influence of  $C_T$  is most pronounced in low- $TI_{\infty}$  and small- $\mathcal{L}_x$  conditions, where clear differences in the shape of the p.d.f. between  $C_T$  cases persist throughout the measurement domain. A similar influence of  $C_T$  on the p.d.f. is observed in the near field for high- $TI_{\infty}$  and large- $\mathcal{L}_x$  cases; however, further downstream, no clear differences are observed. Figure 16(b) further illustrates that wake

meandering is strongly  $C_T$ -dependent in weakly turbulent inflows (with  $\sigma_{y_c}$  increasing with  $C_T$ ) but becomes dominated by ambient turbulence – and thus less sensitive to  $C_T$  – when the background flow is highly turbulent. In addition, a clear influence of  $\mathcal{L}_x$  on  $\sigma_{y_c}/D$  is observed, with FST cases L# exhibiting larger  $\sigma_{y_c}$  at all x/D positions (figure 16c). This increase in  $\sigma_{y_c}$  is further amplified with higher FST intensity. In summary, wake meandering is more pronounced in cases with large- $\mathcal{L}_x$  and high- $TI_{\infty}$ , with the ILS seemingly being the dominant parameter. This aligns with the findings of Kankanwadi & Buxton (2023), who reported increased wake meandering in the wake of a cylinder as the FST ILS increases, as well as with the LES studies of wind turbine wakes by Hodgson et al. (2023) and Vahidi & Porté-Agel (2024), which observed increased wake meandering in wind turbine wakes with both increasing  $\mathcal{L}_x$  and  $TI_{\infty}$ .

Interesting insights into the influence of FST on the wind turbine wake width can be derived by comparing  $\delta(x)$  and  $\sigma_{y_c}(x)$ . In the near field, increasing  $TI_{\infty}$  leads to an increase in  $\delta$  (figure 7) and  $\sigma_{\gamma_c}$  (figure 16), indicating wider time-averaged wakes and enhanced wake meandering. While the influence of  $TI_{\infty}$  on the growth of the instantaneous wake width,  $\delta_i(x,t)$  (figure 8), through entrainment cannot be directly quantified, recent studies on cylinder wakes have reported enhanced near-field entrainment rates with increasing  $TI_{\infty}$  (Kankanwadi & Buxton 2023; Chen & Buxton 2024). Therefore, the increase in the near-field  $\delta$  with  $TI_{\infty}$  may result from both enhanced meandering – leading to an apparent widening of the wake in a time-averaged sense (cf. figure 8) – and an increase in  $\delta_i$  due to enhanced entrainment rates. Conversely, even though farfield wake meandering increases with  $II_{\infty}$  (though plateauing), the reduced time-averaged wake growth rates observed for high- $TI_{\infty}$  cases may be explained by a decrease in the growth of the instantaneous wake width, due to reduced entrainment fluxes in the presence of FST intensity, as reported in cylinder far wakes (Kankanwadi & Buxton 2020; Chen & Buxton 2024). In addition, we previously observed a reduction in the near-field  $\delta$  with increasing FST ILS –  $\delta_{L3,L6} \le \delta_{S4,M5}$  (figure 7) – despite  $\sigma_{\gamma_c}$  increasing, an apparently contradictory result. However, Kankanwadi & Buxton (2023) reported that cylinder wakes exposed to large ILS inflows exhibit enhanced meandering but reduced  $\delta_i$ , resulting in a net decrease in  $\delta$  in the near field  $(x/D \leq 3)$ . By analogy, turbulent inflows with large ILS may lead to a reduction in the instantaneous wind turbine wake width.

We will now investigate wake meandering from the perspective of a low-frequency dynamic. Figure 17 compares the premultiplied power spectra at 4 radial locations,  $y/D \in \{0, 0.5, 1, 2\}$ , and for 4 streamwise positions,  $x/D \in \{2, 5, 10, 20\}$ . The FST spectra, detailed in the Appendix A, are shown in red on each figure, to distinguish the turbine-induced structures from the background turbulence structures. The spectrograms in figure 18 show the streamwise evolution of the energy content of the low-frequency dynamics in the wakes, after subtracting the FST power spectrum  $E_{u'u',0}$ . The resulting quantity,  $\Gamma = E_{u'u'} - E_{u'u',0}$ , isolates the turbine's contribution to the energy content of the low-frequency structures in the wakes. It is important to note that, since  $E_{u'u',0}$  is measured at the hub location,  $\Gamma$  also captures the streamwise decay of the background turbulence structures. However, it can be seen in figure 18(d) that  $\Gamma(x, y/D = 2) \approx 0$  for all x/D, suggesting that the energy content of the background turbulence evolves only marginally along the wind tunnel length.

For all FST cases, a common broad spectral peak within  $St_D \in [0.1, 0.4]$  emerges in the tip shear layer at y/D = 0.5 (figures 17b and 18b). This frequency interval coincides with the Strouhal number range typically reported for wind turbine wake meandering, and is distinct from the FST power spectra. Focusing on the hot-wire at y/D = 0.5, we observe a clear increase in  $E_{u'u'}$  and  $\Gamma$  within that frequency band as  $C_T$  increases, with  $\Gamma_{max}$  occurring closer to the turbine. The existence of wake meandering at  $C_T \approx 0.5$ 

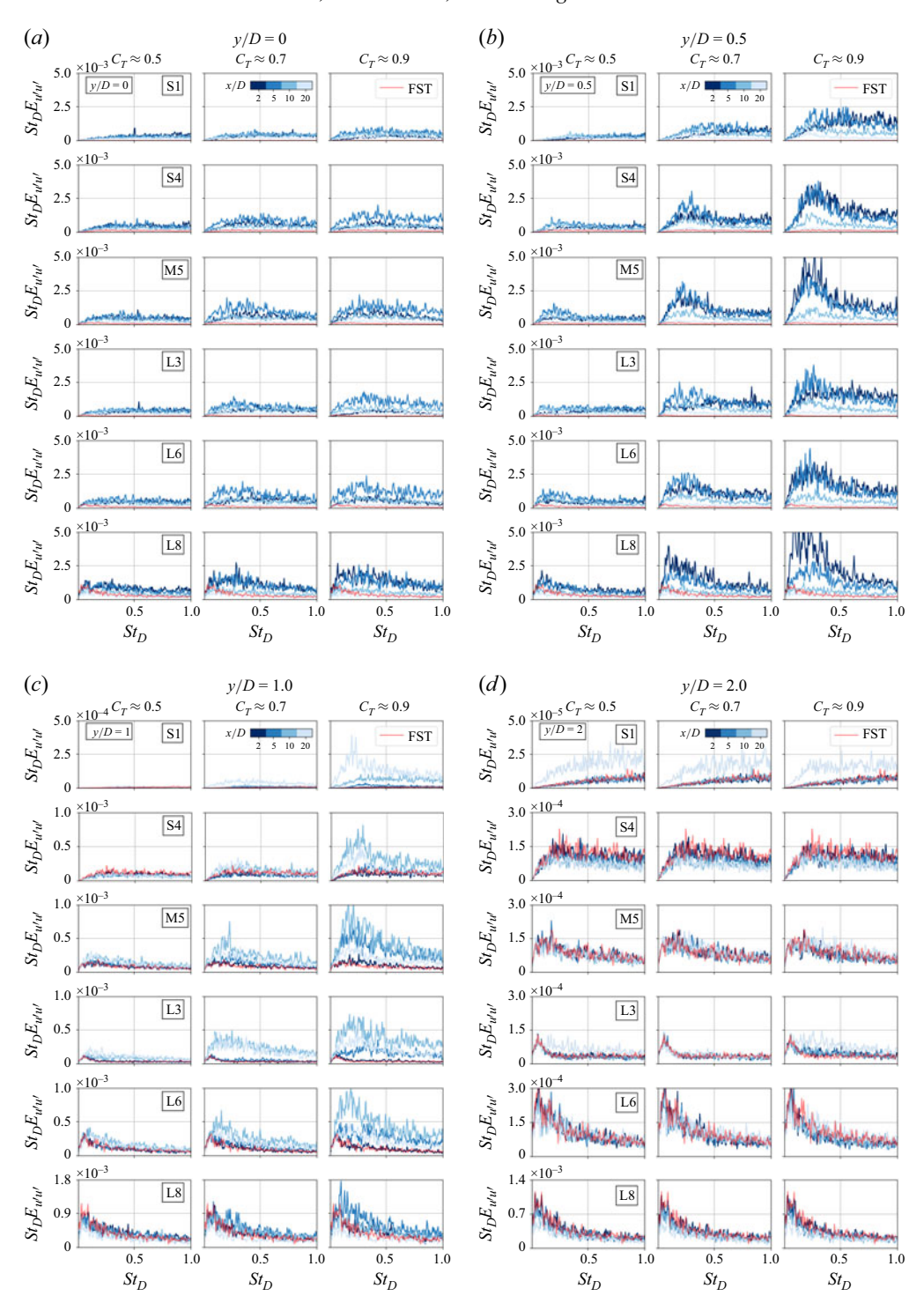


Figure 17. Premultiplied power spectra of the velocity fluctuations,  $St_D E_{u'u'}$ , at y/D = 0 (a), y/D = 0.5 (b), y/D = 1 (c) and y/D = 2 (d), for  $x/D \in \{2, 5, 10, 20\}$ . The Strouhal number is based on the turbine diameter,  $St_D = fD/U_{\infty}$ . The FST power spectra, measured without the turbine at  $\{x/D, y/D\} = \{0, 0\}$ , are shown in red. Note that the ordinate axis scale differs between panels.

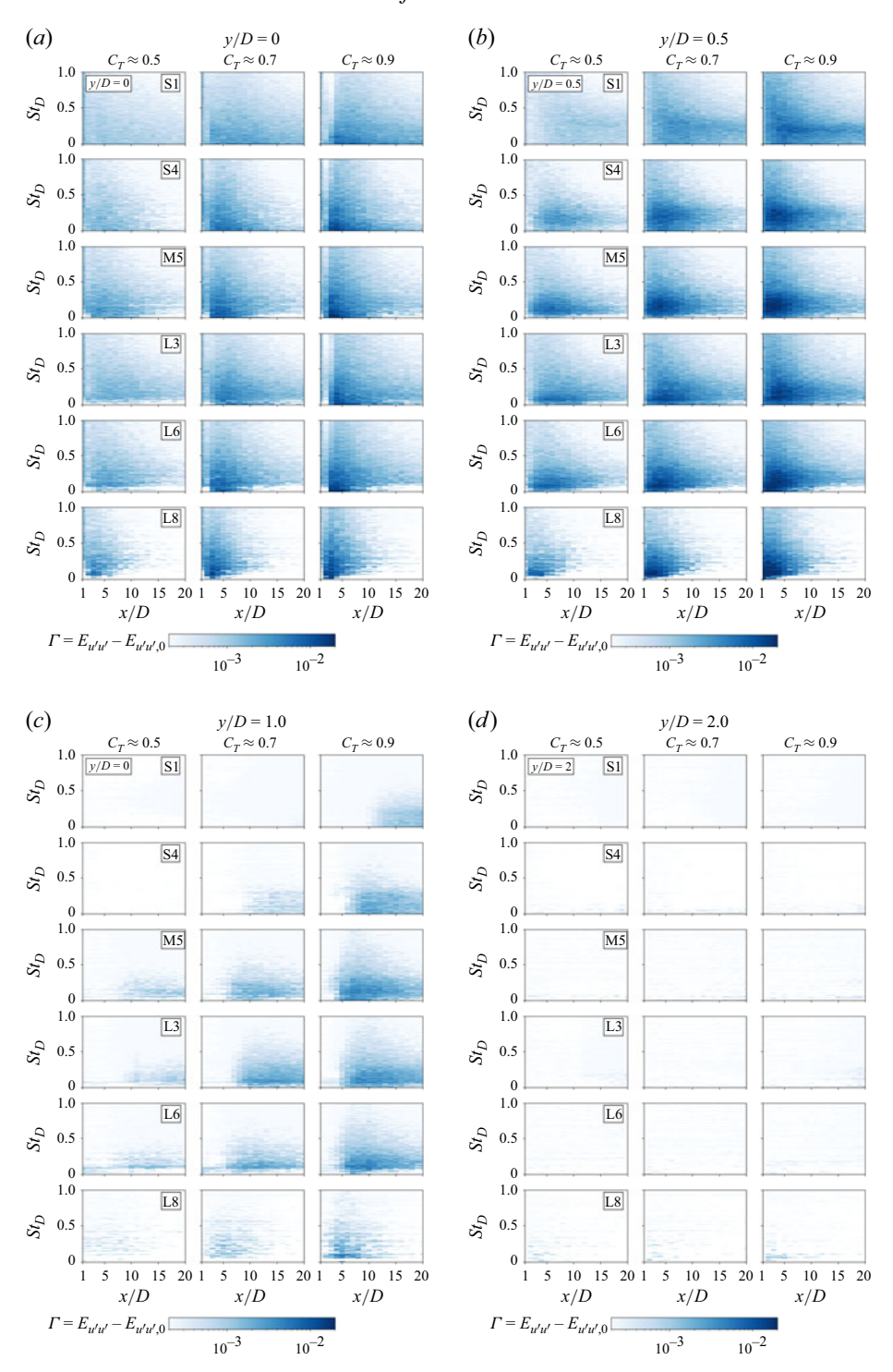


Figure 18. Spectrograms of the velocity fluctuations, expressed as  $\Gamma = E_{u'u'} - E_{u'u',0}$ , at y/D = 0 (a), y/D = 0.5 (b), y/D = 1 (c) and y/D = 2 (d). Here,  $E_{u'u',0}$  denotes the FST power spectra measured at  $\{x/D, y/D\} = \{0, 0\}$  without the turbine. The Strouhal number is based on the turbine diameter,  $St_D = fD/U_\infty$ .

is questionable, particularly in the lowest turbulence cases, S1 and S2. This behaviour mirrors vortex shedding from porous bodies, which occurs only above a certain porosity threshold and whose strength increases with reduced porosity (Cannon, Champagne & Glezer 1993; Bourhis & Buxton 2024). In addition, both  $E_{u'u'}$  and  $\Gamma$  within  $St_D \in [0.1, 0.4]$  increase with  $TI_{\infty}$  and  $\mathcal{L}_x$ , aligning with the previous observation of increased  $\sigma_{y_c}$ . Higher  $TI_{\infty}$  also results in a broadening of the wake meandering frequency range. Moreover, while a clear broad peak is observed for group 2 and 3 FST cases, it is less distinct for group 1 cases, highlighting the influence of FST in either triggering or at least enhancing wake meandering. The streamwise location x/D where  $E_{u'u'}$  and  $\Gamma$  are maximised shifts closer to the turbine as  $TI_{\infty}$  increases. Moreover, while  $\Gamma(St_D \in [0.1, 0.4])$  increases in the near field with higher  $TI_{\infty}$ , it decays more rapidly downstream (e.g.  $\Gamma_{L3}(y/D = 0.5) \geqslant \Gamma_{L6}(y/D = 0.5)$  for  $x/D \geqslant 10$ ).

Interestingly, for small ILS inflows (S1, S2 and S4), a peak in  $\mathcal{L}_x$  was previously identified in the tip shear layer (figure 6), becoming more pronounced and shifting radially downstream as the wakes developed, highlighting the growth of coherent structures. This broad peak coincides with an increase in  $E_{u'u'}(St_D \in [0.1, 0.4])$  that first emerges in the tip shear layer (see y/D = 0.5 in figure 17b), before extending to larger radial positions (see y/D = 1.0 in figure 17c), ultimately mirroring the ILS evolution. The correspondence between increased ILS and the peak in  $E_{u'u'}(St_D \in [0.1, 0.4])$  within the tip shear layer indicates that, for cases S#, wake meandering is primarily driven by flow structures originating in the tip shear layer, thereby supporting the shear-layer-driven wake meandering mechanism. Moreover, the concurrent increase in  $\sigma_{y_c}$ ,  $E_{u'u'}$  and  $\Gamma$  with  $C_T$  correlates with the growth of  $\mathcal{L}_x$  in the tip shear layer at higher  $C_T$ , further emphasising the role of turbine-induced coherent flow structures on the meandering of the wakes. Specifically, higher  $C_T$  leads to higher flow blockage by the turbine and a stronger tip shear layer, thereby promoting the development of more energetic flow structures emerging from shear-layer instability, which ultimately enhance wake meandering. However, as highlighted in figure 16, the lateral wake displacements remain small for these weakly turbulent inflows (small  $\sigma_{v_c}$ ).

Similarly, for cases with large- $\mathcal{L}_x$  and high- $TI_{\infty}$ , a broad peak in  $E_{u'u'}(St_D \in [0.1, 0.4])$  emerges in the tip shear layer, with its amplitude increasing with both  $C_T$  and  $TI_{\infty}$ . This indicates that FST introduces more energy in the large-scale structures within the tip shear layer, which may intensify shear-layer-driven wake meandering and partly account for the increase in  $\sigma_{y_c}$  (figure 16). However, for cases L7 and L8, the increase in  $E_{u'u'}(St_D \in [0.1-0.4])$  at higher  $C_T$  does not translate into an increase in  $\sigma_{y_c}$ , i.e. in wake displacement. Moreover, when comparing cases S4 and L3, we observe  $\sigma_{y_c,L3} \geqslant \sigma_{y_c,S4}$  despite  $E_{u'u'}(St_D \in [0.1, 0.4])$  being larger in case S4. Taken together, these results suggest that in highly turbulent inflows, shear-layer-driven wake meandering is not the only mechanism responsible for the large-scale motion of the wake; large-scale background eddies may also play an important role in driving lateral wake displacements. Notably, as  $TI_{\infty}$  and  $\mathcal{L}_x$  increase, the influence of  $C_T$  progressively diminishes, suggesting a shift in the dominant mechanism of wake meandering from a shear-layer instability towards a stronger role of large-scale ambient eddies.

Moreover, for large- $\mathcal{L}_x$  and high- $TI_{\infty}$  cases, the peak energy content  $St_D \in [0.1, 0.4]$  is observed immediately downstream of the turbine, after which the associated structure rapidly decays and becomes negligible compared with the low-frequency background turbulence. Therefore, we may postulate that, in the far field, the large wake displacements captured by  $\sigma_{y_c}$  are predominantly driven by the large eddies in the ambient flow. As the wake develops, both  $\Gamma(St_D \in [0.1, 0.4])$  and  $E_{u'u'}(St_D \in [0.1, 0.4])$  at y/D = 1 progressively increase (figures 17c and 18c), although both are smaller than at y/D = 0.5,

with their maxima occurring further in the wake. This highlights the spreading and diffusion of these low-frequency structures as the wakes develop. Finally, at the hot-wire position furthest from the wake centreline (y/D=2), the spectra for each FST case are qualitatively similar across the streamwise measurement locations, and  $\Gamma \approx 0$ , indicating that ambient structures dominate at this location, except for case S1, where the increase in  $E_{u'u'}(x/D=20)$  emphasises the presence of the turbine's wake (figures 17d and 18d).

In summary, the spectral analysis suggests that wake meandering originates from a tip shear-layer instability, as evidenced by the broad spectral peak in  $St_D \in [0.1, 0.4]$ observed within the tip shear region. Additionally, wake meandering exhibits similar characteristics to vortex shedding from bluff and porous bodies, particularly in low- $TI_{\infty}$  and small- $\mathcal{L}_x$  inflows: it manifests only above a certain porosity (e.g. sufficiently high  $C_T$  and  $\Lambda$ ); FST broadens its frequency band, enhances near-wake energy content and accelerates downstream decay - consistent with the established influence of FST on vortex shedding (Bourhis & Buxton 2024; de Oliveira, Sharif Khodaei & Buxton 2025). Moreover, wake meandering is strongly modulated by FST, with both  $TI_{\infty}$  and  $\mathcal{L}_x$ amplifying the large-scale wake motion (i.e. increasing  $\sigma_{v_c}$ ) and enhancing the spectral energy content within  $St_D \in [0.1, 0.4]$ . In weakly turbulent inflows (e.g. S1, S2), wake meandering is driven primarily by turbine-related coherent structures originating in the tip shear layer and results in limited lateral wake displacements, which are sensitive to variations in  $C_T$  and  $\Lambda$ . Conversely, under highly turbulent inflow conditions, the influence of  $C_T$  becomes negligible, and ambient turbulence appears to drive the largescale wake motion, especially in the far field. These findings suggest that wind turbine wake meandering cannot be attributed exclusively to the passive advection of the wake by large structures in the ambient flow, as hypothesised in the DWM model, nor to shear-layer instabilities analogous to vortex shedding from bluff bodies. Rather, both mechanisms likely coexist, with their respective contributions depending on the FST conditions.

# 4. Summary and conclusions

An in-depth experimental investigation was conducted to assess the influence of FST on wind turbine-generated wakes over an extended streamwise distance and at high Reynolds numbers. The FST intensity (1 %  $\lesssim TI_{\infty} \lesssim$  11 %) and ILS (0.1  $\lesssim \mathcal{L}_x/D \lesssim$  2) along with the turbine thrust coefficient ( $C_T \in \{0.5, 0.7, 0.9\}$ ) were independently varied across a broad range representative of typical real-world wind turbine operating conditions.

First, it was observed that a wake defined as a flow region of increased turbulence intensity and TKE vanishes earlier than a wake defined as a flow region of reduced mean momentum. Specifically, for high- $TI_{\infty}$  inflows, a flow region was identified in the far field, where the velocity deficit remains, despite the TKE having already homogenised with that of the free stream, challenging conventional wake definitions established for non-turbulent inflows. Beyond this location, the decay of the velocity deficit slows, and a pronounced reduction in the wake growth rate is observed. This emphasises the enhanced entrainment rate of TKE relative to mass and momentum, particularly in the near field – a phenomenon also observed in the near wake of bluff bodies exposed to FST (Buxton & Chen 2023). While Gaussian-like velocity deficit profiles, and saddle-shape TKE profiles, are observed in the far field for low- $TI_{\infty}$  cases – typical of a self-similar evolution for axisymmetric wakes – the presence of high ambient  $TI_{\infty}$  suppresses the possibility of such self-similar evolution, as also reported in bluff-body far wakes (Rind & Castro 2012). The turbine acts as a high-pass filter to the large structures present in the inflows, with a higher  $C_T$ leading to an increased blocking of these structures, mirroring the behaviour of porous discs with decreasing porosity (Bourhis & Buxton 2024). For inflows with a large FST ILS,

the ILS within the wake recovers and gradually aligns with that of the background flow. For inflows with a small ILS, the largest structures in the flow are those introduced by the turbine, originating from the tip shear layer and expanding radially as the wake develops. Moreover, akin to porous bodies, the size and strength of these structures increase with  $C_T$ , i.e. as the turbine porosity decreases.

Second, a novel finding is the significant change in the slope of the wake width evolution, particularly for wakes exposed to high FST intensity and large ILS. A clear turning point was observed in highly turbulent cases (L7, L8), beyond which the wake width plateaus and the growth rate decreases substantially. This plateau phase starts closer to the turbine, with a progressively sharper transition as  $TI_{\infty}$  increases, and appears to coincide with the location at which the turbine-added TKE has nearly fully dissipated. In the near field  $(x/D \lesssim 7)$ , the wake width increases with  $C_T$ ,  $TI_{\infty}$  and  $\mathcal{L}_x$ . While the wake growth rate also increases with  $C_T$  and  $TI_{\infty}$ , the influence of the ILS is negligible. However, in the far field  $(x/D \gtrsim 15)$ , a significant reduction in the wake growth rate is observed with increasing  $TI_{\infty}$ . While these results represent a novel contribution to wind turbine wake literature, they align with the entrainment behaviours observed in bluff- and porous-body wakes. Specifically, they are consistent with prior studies showing reduced entrainment rates in the far wake of porous bodies (Vinnes *et al.* 2023; Bourhis & Buxton 2024) and bluff bodies (Kankanwadi & Buxton 2020; Chen & Buxton 2023, 2024) exposed to FST, as  $TI_{\infty}$  increases.

Third, it was found that increasing  $TI_{\infty}$  enhances the recovery of the velocity and the dissipation of the turbine-added TKE, with the wake recovery starting closer to the turbine, whereas larger  $\mathcal{L}_x$  tends to delay its onset. For high- $TI_{\infty}$  inflows, the turbulence within the wakes tends to adjust rapidly to the background turbulence, with the influence of  $C_T$  diminishing quickly. In contrast, for low- $TI_{\infty}$  inflows, where turbine-generated turbulence dominates the wake dynamics, near-wake modifications arising from variations in  $C_T$  persist into the far field.

Fourth, we found that the turbine operating point  $\{\Lambda, C_T\}$  primarily determines the presence or absence of certain near-field dynamics, while FST acts on the near-field dynamics energy decay. These dynamics persist longer in the wake in low- $TI_{\infty}$  conditions but dissipate rapidly in high- $TI_{\infty}$  conditions, with a negligible influence of the ILS.

Fifth, the statistical and dynamic characteristics of wake meandering were examined. For most  $\{C_T, FST\}$  cases, a broad spectral peak characteristic of wake meandering  $(St_D \approx$ 0.2) was observed to originate in the tip shear layer, supporting shear-layer instability as a triggering mechanism. In low- $TI_{\infty}$  and small- $\mathcal{L}_x$  inflows, however, the resulting lateral motions were found to be very limited, suggesting that shear-layer-driven meandering alone does not translate into substantial large-scale wake displacement. In contrast, inflows with large FST intensities and ILS significantly amplify the wake's lateral motions, with the ILS playing a leading role, as also reported for bluff bodies (Kankanwadi & Buxton 2023). Hence, while shear-layer-driven wake meandering may occur in both laminar and turbulent inflows, the amplitude of the large-scale wake motion becomes significant only in the presence of FST. This aligns with the LES of wind turbine wakes by Li et al. (2022), who found that wake meandering in high- $II_{\infty}$  inflows was dominated by ambient turbulence. Finally, although increasing  $C_T$  (and  $\Lambda$ ) enhances wake meandering in weakly turbulent inflows - consistent with findings on porous-disc wakes (Bourhis & Buxton 2024) – its influence becomes negligible in strongly turbulent inflows, highlighting the interplay between ambient flow turbulence and the turbine operating point in driving this dynamic.

In conclusion, this work is one of the first experimental studies to examine wind turbine wakes over such long distances and across a broad range of FST conditions and thrust

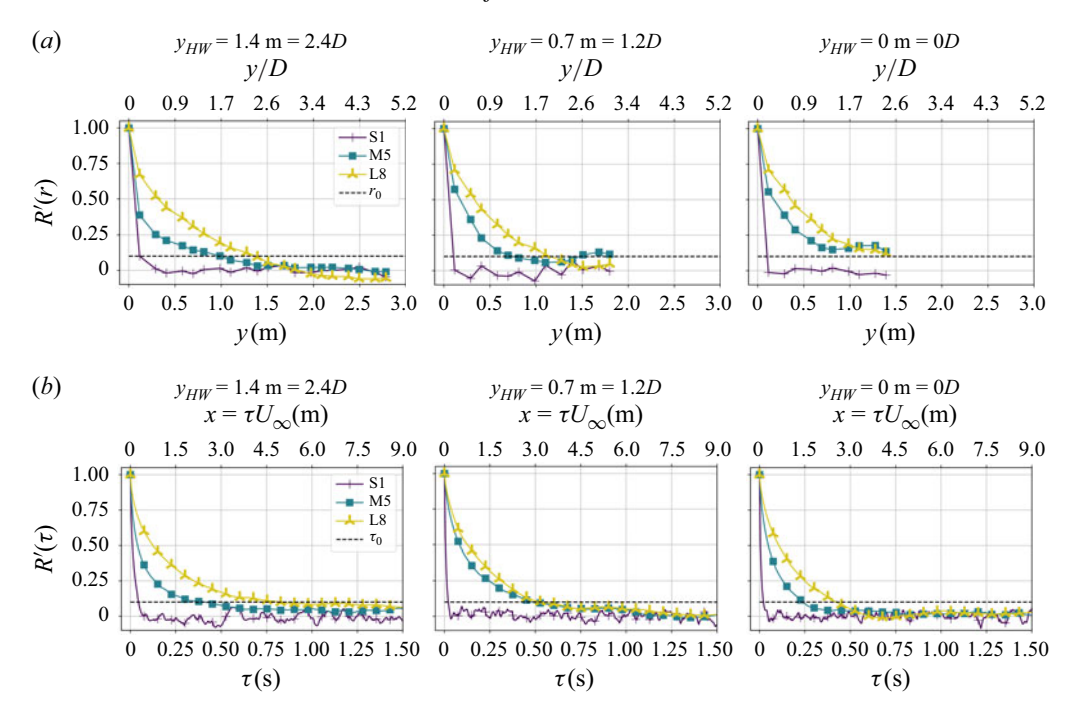


Figure 19. Spatial R'(r) (a) and temporal  $R'(\tau)$  (b) normalised autocorrelation functions of the fluctuating velocity u' computed at  $\{x/D, z/D\} = \{0, 0\}$  for three different radial positions y/D along the wind tunnel width and for three FST cases.

coefficients, covering a parametric space with  $24 \{C_T, FST\}$  configurations. Notably, most studies on the impact of turbulence length scales on wakes have been carried out using LES or with smaller bluff bodies – such as cylinders and discs – due to physical constraints in generating large turbulence length scales in wind tunnels. The distinct roles of the thrust coefficient, turbulence intensity and ILS in wake turbulence statistics and dynamics – both near and far from the turbine – are emphasised, also highlighting the spatial dependence of these effects. Finally, several parallels were drawn with the wakes of wind turbine surrogates, such as porous discs, revealing that similar physical mechanisms govern the wakes of both bluff bodies and wind turbines. Notably, the reduced wake growth rates observed in the far field with increasing FST intensity, along with similarities in the tip shear-layer dynamics, help bridge current understanding of wind turbine wakes with research on bluff- and porous-body wakes.

Supplementary movies. Supplementary movies are available at https://doi.org/10.1017/jfm.2025.10788.

Acknowledgements. The authors would like to acknowledge J. Jüchter and L. Neuhaus for their valuable help with the experiments.

**Funding.** The authors gratefully acknowledge the Engineering and Physical Sciences Research Council (EPSRC) for funding this work through grant no. EP/V006436/1.

**Declaration of interests.** The authors report no conflict of interest. For the purposes of open access, the authors have applied a Creative Commons Attribution (CC BY) licence to any Author Accepted Manuscript (AAM) version arising.

#### Appendix A. Characteristics of the different turbulent inflows

This appendix provides further details on the characteristics of the different turbulent inflows generated by the active grid. The 8 inflows were characterised across the

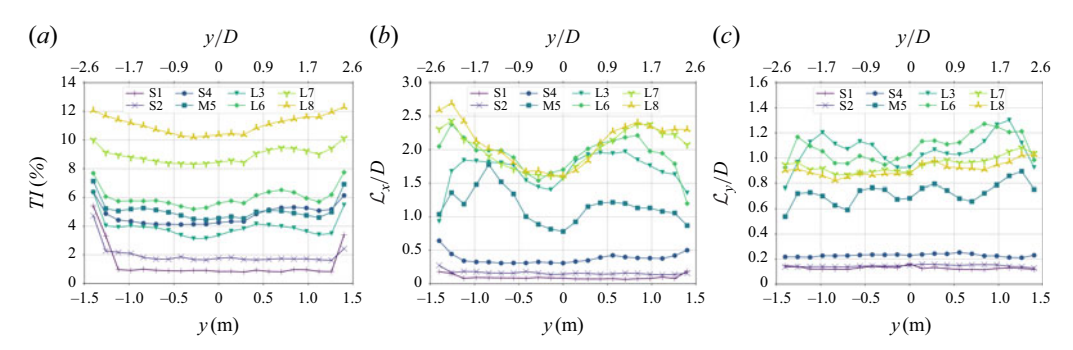


Figure 20. Profiles of turbulence intensity TI (%) (a), streamwise ILS  $\mathcal{L}_x/D$  (b) and spanwise ILS  $\mathcal{L}_y/D$  (c), computed at  $\{x/D, z/D\} = \{0, 0\}$ .

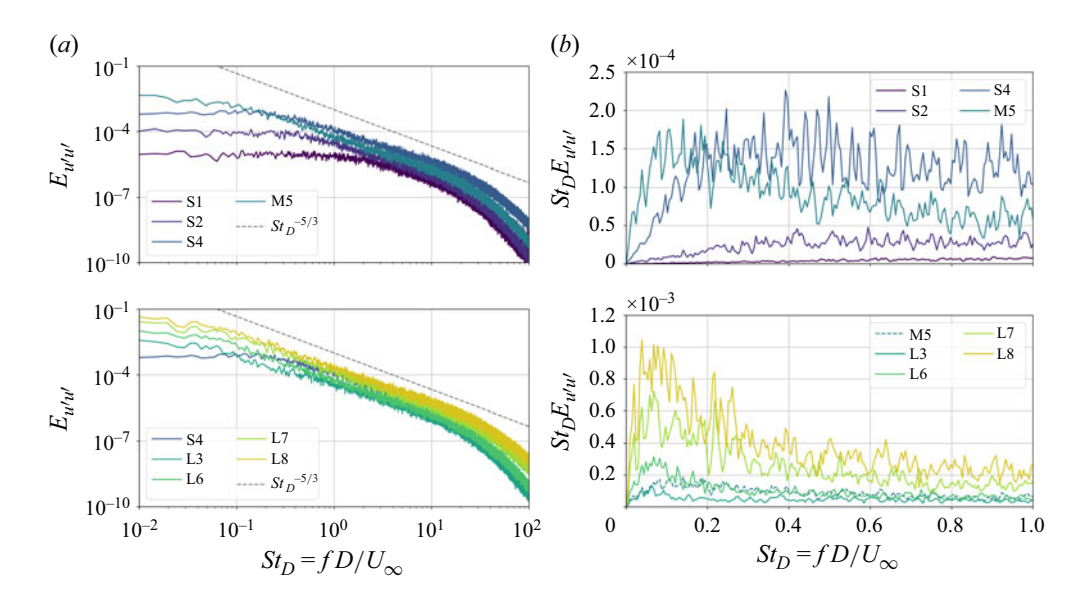


Figure 21. The FST power spectra,  $E_{u'u'}$ , (a) and premultiplied power spectra,  $St_D E_{u'u'}$ , (b) of the velocity fluctuations u', as a function  $St_D = fD/U_{\infty}$ . Spectra are computed at the hub centre location  $\{x/D, y/D, z/D\} = \{0, 0, 0\}$ . A particular focus is placed on the low-frequency dynamics in the premultiplied spectra ( $St_D \in [0, 1]$ ).

width of the wind tunnel at the turbine's location, i.e. along the horizontal axis y at  $\{x/D, z/D\} = \{0, 0\}$ . Figure 19 presents the normalised spatial and temporal autocorrelation functions of the velocity fluctuations u', for different horizontal positions and FST cases. Figure 20 shows the profiles of turbulence intensity and ILSs. Finally, the FST spectra and premultiplied spectra of the velocity fluctuations are provided in figure 21.

#### Appendix B. Wind turbine operating points

Table 2 presents the time-averaged thrust coefficients and tip-speed ratios for all FST cases. The measured  $C_T$  values represent the total load acting on the turbine, including the nacelle, tower and blades. In a previous study, Neunaber *et al.* (2020) estimated that the tower and nacelle of the MoWito 0.6, without the blades, account for 17% of the total measured thrust. The variations in  $C_T$  and  $\Lambda$  across the FST cases are negligible, suggesting that both parameters are largely insensitive to  $TI_{\infty}$  and  $\mathcal{L}_x$ .

FST case	Low	$C_T$	Mediu	$\text{im-}C_T$	$High-C_T$	
	$C_T$	$\Lambda$	$C_T$	Λ	$C_T$	Λ
S1	0.47	1.63	0.67	2.56	0.89	3.78
S2	0.46	1.70	0.62	2.85	0.89	3.56
S4	0.48	1.73	0.71	2.71	0.92	3.68
M5	0.48	1.70	0.69	2.70	0.89	3.67
L3	0.48	1.73	0.67	2.66	0.89	3.80
L6	0.49	1.76	0.70	2.69	0.88	3.60
L7	0.49	1.71	0.69	2.60	0.91	3.68
L8	0.47	1.70	0.69	2.61	0.91	3.68

Table 2. Time-averaged thrust coefficients and tip-speed ratios for the 24 combinations.

#### REFERENCES

- ARGYLE, P., WATSON, S., MONTAVON, C., JONES, I. & SMITH, M. 2018 Modelling turbulence intensity within a large offshore wind farm. *Wind Energy* **21** (12), 1329–1343.
- BARTHELMIE, R.J. & JENSEN, L.E. 2010 Evaluation of wind farm efficiency and wind turbine wakes at the Nysted offshore wind farm. *Wind Energy* 13 (6), 573–586.
- BASTANKHAH, M. & PORTÉ-AGEL, F. 2014 A new analytical model for wind-turbine wakes. *Renew. Energy* **70**, 116–123.
- BISWAS, N. & BUXTON, O.R.H. 2024a Effect of tip speed ratio on coherent dynamics in the near wake of a model wind turbine. *J. Fluid Mech.* **979**, A34.
- BISWAS, N. & BUXTON, O.R.H. 2024b Energy exchanges between coherent modes in the near wake of a wind turbine model at different tip speed ratios. *J. Fluid Mech.* **996**, A8.
- BLACKMORE, T., BATTEN, W.M.J. & BAHAJ, A.S. 2014 Influence of turbulence on the wake of a marine current turbine simulator. *Proc. R. Soc. Lond. A* 470, 20140331.
- BOURHIS, M. & BUXTON, O.R.H. 2024 Influence of freestream turbulence and porosity on porous diskgenerated wakes. *Phys. Rev. Fluids* 9 (12), 124501.
- BOURHIS, M., PEREIRA, M. & RAVELET, F. 2023 Experimental investigation of the effects of the Reynolds number on the performance and near wake of a wind turbine. *Renew. Energy* **209**, 63–70.
- BURTON, T.L., JENKINS, N., BOSSANYI, E., SHARPE, D. & GRAHAM, M. 2021 The wind resource. In *Wind Energy Handbook*, 3rd edn, chap. 2, pp. 11–38. John Wiley & Sons, Ltd.
- BUXTON, O.R.H. & CHEN, J. 2023 The relative efficiencies of the entrainment of mass, momentum and kinetic energy from a turbulent background. *J. Fluid Mech.* 977, R2.
- CAL, R.B., LEBRÓN, J., CASTILLO, L., KANG, H.S. & MENEVEAU, C. 2010 Experimental study of the horizontally averaged flow structure in a model wind-turbine array boundary layer. J. Renew. Sustain. Energy 2 (1), 013106.
- CANNON, S., CHAMPAGNE, F. & GLEZER, A. 1993 Observations of large-scale structures in wakes behind axisymmetric bodies. *Exp. Fluids: Expl Met. Applics Fluid Flow* **14** (6), 447–450.
- CARBAJO FUERTES, F., MARKFORT, C.D. & PORTÉ-AGEL, F. 2018 Wind turbine wake characterization with nacelle-mounted wind lidars for analytical wake model validation. *Remote Sens.* 10 (5), 668.
- CHAMORRO, L.P., ARNDT, R.E.A. & SOTIROPOULOS, F. 2012a Reynolds number dependence of turbulence statistics in the wake of wind turbines. *Wind Energy* 15 (5), 733–742.
- CHAMORRO, L., GUALA, M., ARNDT, R. & SOTIROPOULOS, F. 2012b On the evolution of turbulent scales in the wake of a wind turbine model. *J. Turbul.* 13, N27.
- CHAMORRO, L.P. & PORTÉ-AGEL, F. 2009 A wind-tunnel investigation of wind-turbine wakes: boundary-layer turbulence effects. Boundary-Layer Meteorol. 132 (1), 129–149.
- CHEN, J. & BUXTON, O.R.H. 2023 Spatial evolution of the turbulent/turbulent interface geometry in a cylinder wake. J. Fluid Mech. 969, A4.
- CHEN, J. & BUXTON, O.R.H. 2024 Turbulent/turbulent entrainment in a planar wake. J. Fluid Mech. 1000, A26.
- CHENG, Y., ZHANG, M., ZHANG, Z. & Xu, J. 2019 A new analytical model for wind turbine wakes based on Monin-Obukhov similarity theory. Appl. Energy 239, 96–106.
- CICOLIN, M.M., CHELLINI, S., USHERWOOD, B., GANAPATHISUBRAMANI, B. & CASTRO, I.P. 2024 Vortex shedding behind porous flat plates normal to the flow. *J. Fluid Mech.* **985**, A40.

- Dong, G., Qin, J., Li, Z. & Yang, X. 2023 Characteristics of wind turbine wakes for different blade designs. J. Fluid Mech. 965, A15.
- Du, B., GE, M., ZENG, C., Cui, G. & Liu, Y. 2021 Influence of atmospheric stability on wind-turbine wakes with a certain hub-height turbulence intensity. *Phys. Fluids* **33** (5), 055111.
- FELLI, M., CAMUSSI, R. & DI FELICE, F. 2011 Mechanisms of evolution of the propeller wake in the transition and far fields. *J. Fluid Mech.* **682**, 5–53.
- GAMBUZZA, S. & GANAPATHISUBRAMANI, B. 2023 The influence of freestream turbulence on the development of a wind turbine wake. *J. Fluid Mech.* 963, A19.
- HEARST, R.J. & GANAPATHISUBRAMANI, B. 2017 Tailoring incoming shear and turbulence profiles for labscale wind turbines. *Wind Energy* **20** (12), 2021–2035.
- HODGSON, E.L., AA MADSEN, M.H., TROLDBORG, N. & ANDERSEN, S.J. 2022 Impact of turbulent time scales on wake recovery and operation. J. Phys.: Conf. Ser. 2265 (2), 022022.
- HODGSON, E.L., MADSEN, M.H.A. & ANDERSEN, S.J. 2023 Effects of turbulent inflow time scales on wind turbine wake behavior and recovery. *Phys. Fluids* **35** (9), 095125.
- HULSMAN, P., WOSNIK, M., PETROVIĆ, V., HÖLLING, M. & KÜHN, M. 2022 Development of a curled wake of a yawed wind turbine under turbulent and sheared inflow. *Wind Energy Sci.* 7 (1), 237–257.
- IEC 2019 Iec 61400-3, wind energy generation systems-part 3-1: design requirements for fixed offshore wind turbines. Tech. Rep.. International Electrotechnical Commission, Geneva.
- ISHIHARA, T. & QIAN, G.-W. 2018 A new gaussian-based analytical wake model for wind turbines considering ambient turbulence intensities and thrust coefficient effects. J. Wind Engng Ind. Aerodyn. 177, 275–292.
- JENSEN, N.O. 1983 A note on wind generator interaction. Risø-M No. 2411. Risø National Laboratory.
- KANKANWADI, K.S. & BUXTON, O.R.H. 2020 Turbulent entrainment into a cylinder wake from a turbulent background. J. Fluid Mech. 905, A35.
- KANKANWADI, K.S. & BUXTON, O.R.H. 2023 Influence of freestream turbulence on the near-field growth of a turbulent cylinder wake: turbulent entrainment and wake meandering. *Phys. Rev. Fluids* 8 (3), 034603.
- KIRBY, A., NISHINO, T., LANZILAO, L., DUNSTAN, T.D. & MEYERS, J. 2025 Turbine- and farm-scale power losses in wind farms: an alternative to wake and farm blockage losses. *Wind Energy Sci.* **10** (2), 435–450.
- LARSEN, G.C., MADSEN, H.A., THOMSEN, K. & LARSEN, T.J. 2008 Wake meandering: a pragmatic approach. Wind Energy 11 (4), 377–395.
- LI, Y., ZHANG, F., LI, Z. & YANG, X. 2024 Impacts of inflow turbulence on the flow past a permeable disk. J. Fluid Mech. 999, A30.
- LI, Z., DONG, G. & YANG, X. 2022 Onset of wake meandering for a floating offshore wind turbine under side-to-side motion. J. Fluid Mech. 934, A29.
- LIGNAROLO, L.E.M., RAGNI, D., KRISHNASWAMI, C., CHEN, Q., FERREIRA, C.J.S. & VAN BUSSEL, G.J.W. 2014 Experimental analysis of the wake of a horizontal-axis wind-turbine model. *Renew. Energy* 70, 31–46.
- LINGKAN, E.H. & BUXTON, O.R.H. 2023 An assessment of the scalings for the streamwise evolution of turbulent quantities in wakes produced by porous objects. *Renew. Energy* **209**, 1–9.
- MESSMER, T., HÖLLING, M. & PEINKE, J. 2024 Enhanced recovery caused by nonlinear dynamics in the wake of a floating offshore wind turbine. *J. Fluid Mech.* **984**, A66.
- MORTENSEN, N.G., HEATHFIELD, D.N., MYLLERUP, L., LANDBERG, L. & RATHMANN, O. 2007 Wind Atlas Analysis and Application Program: WASP 9 help Facility. Danmarks Tekniske Universitet, Risø Nationallaboratoriet for Bæredygtig Energi.
- NEUHAUS, K., BERGER, F., PEINKE, J. & HÖLLING, M. 2021 Exploring the capabilities of active grids. *Exp. Fluids* **62** (6), 130.
- NEUHAUS, L., HÖLLING, M., BOS, W.J.T. & PEINKE, J. 2020 Generation of atmospheric turbulence with unprecedentedly large Reynolds number in a wind tunnel. *Phys. Rev. Lett.* **125** (15), 154503.
- NEUNABER, I., HÖLLING, M., STEVENS, R.J.A.M., SCHEPERS, G. & PEINKE, J. 2020 Distinct turbulent regions in the wake of a wind turbine and their inflow-dependent locations: the creation of a wake map. *Energies* 13 (20), 5392.
- NIAYIFAR, A. & PORTÉ-AGEL, F. 2016 Analytical modeling of wind farms: a new approach for power prediction. *Energies* 9 (9), 741.
- OKULOV, V.L. & SØRENSEN, J.N. 2007 Stability of helical tip vortices in a rotor far wake. *J. Fluid Mech.* **576**, 1–25.
- DE OLIVEIRA, F.J.G., SHARIF KHODAEI, Z. & BUXTON, O.R.H. 2025 The influence of free-stream turbulence on the fluctuating loads experienced by a cylinder exposed to a turbulent cross-flow. *J. Fluid Mech.* 1011, A47.
- PEÑA, A., FLOORS, R., SATHE, A., GRYNING, S.-E., WAGNER, R., COURTNEY, M.S., LARSÉN, X.G., HAHMANN, A.N. & HASAGER, C.B. 2016 Ten years of boundary-layer and wind-power meteorology at Høvsøre, Denmark. *Boundary-Layer Meteorol.* **158** (1), 1–26.

- PORTÉ-AGEL, F., BASTANKHAH, M. & SHAMSODDIN, S. 2019 Wind-turbine and wind-farm flows: a review. Boundary-Layer Meteorol. 174, 1–59.
- RIND, E. & CASTRO, I.P. 2012 On the effects of free-stream turbulence on axisymmetric disc wakes. *Exp. Fluids* **53**, 301–318.
- ROCKEL, S., PEINKE, J., HÖLLING, M. & CAL, R.B. 2017 Dynamic wake development of a floating wind turbine in free pitch motion subjected to turbulent inflow generated with an active grid. *Renew. Energy* 112, 1–16
- SHERRY, M., NEMES, A., JACONO, D.L., BLACKBURN, H.M. & SHERIDAN, J. 2013 The interaction of helical tip and root vortices in a wind turbine wake. *Phys. Fluids* **25** (11), 117102.
- STEVENS, R.J.A.M. & MENEVEAU, C. 2017 Flow structure and turbulence in wind farms. *Annu. Rev. Fluid Mech.* 49, 311–339.
- THOMSEN, K. & SØRENSEN, P. 1999 Fatigue loads for wind turbines operating in wakes. J. Wind Engng Ind. Aerodyn. 80 (1), 121–136.
- VAHIDI, D. & PORTÉ-AGEL, F. 2024 Influence of incoming turbulent scales on the wind turbine wake: a large-eddy simulation study. *Phys. Fluids* 36 (9), 095177.
- VAHIDI, D. & PORTÉ-AGEL, F. 2025 Influence of thrust coefficient on the wake of a wind turbine: a numerical and analytical study. *Renew. Energy* **240**, 122194.
- VAN DER DEIJL, W., SCHMITT, F., SICOT, C., BARRE, S., HÖLLING, M. & OBLIGADO, M. 2024 Effect of background turbulence on the wakes of horizontal-axis and vertical-axis wind turbines. *J. Wind Engng Ind. Aerodyn.* 253, 105877.
- VERMEER, L.J., SØRENSEN, J.N. & CRESPO, A. 2003 Wind turbine wake aerodynamics. Prog. Aerosp. Sci. 39 (6), 467–510.
- VINNES, M.K., NEUNABER, I., LYKKE, H.M.H. & HEARST, R.J. 2023 Characterizing porous disk wakes in different turbulent inflow conditions with higher-order statistics. *Exp. Fluids* **64** (2), 1–16.
- YANG, X. & SOTIROPOULOS, F. 2019 A review on the meandering of wind turbine wakes. *Energies* 12 (24), 4725.
- ZHANG, F., YANG, X. & HE, G. 2023 Multiscale analysis of a very long wind turbine wake in an atmospheric boundary layer. *Phys. Rev. Fluids* 8, 104605.
- ZHOU, N., CHEN, J., ADAMS, D.E. & FLEETER, S. 2016 Influence of inflow conditions on turbine loading and wake structures predicted by large eddy simulations using exact geometry. *Wind Energy* **19** (5), 803–824.